

# Mathematical Modelling of Mechanotransduction via RhoA Signalling Pathways

Sofie Verhees<sup>1</sup>, Chandrasekhar Venkataraman<sup>2</sup>, Mariya Ptashnyk<sup>1</sup>

<sup>1</sup>Department of Mathematics, Heriot-Watt University, The Maxwell Institute for Mathematical Sciences, Edinburgh; <sup>2</sup>Department of Mathematics, University of Sussex, Brighton

## Abstract

We derive and simulate a mathematical model for mechanotransduction related to the Rho GTPase signalling pathway. The model addresses the bidirectional coupling between signalling processes and cell mechanics. A numerical method based on bulk-surface finite elements is proposed for the approximation of the coupled system of nonlinear reaction-diffusion equations, defined inside the cell and on the cell membrane, and the equations of elasticity. Our simulation results illustrate novel emergent features such as the strong dependence of the dynamics on cell shape, a threshold-like response to changes in substrate stiffness, and the fact that coupling mechanics and signalling can lead to the robustness of cell deformation to larger changes in substrate stiffness, ensuring mechanical homeostasis in agreement with experiments.

**Keywords:** mechanotransduction, bulk-surface finite elements, cell signalling

## 1 Introduction

Intercellular signalling processes constitute the mechanisms through which cells communicate with and respond to their environment. Hence, signalling pathways are important in all physiological activities of the cell, such as cell division, cell movement, the immune response, and tissue development [Tom+09]. Aberrant cell signalling can often result in the development of diseases [VE22]. It is therefore important to understand signalling phenomena. Recent studies have found that alongside biochemical reactions, mechanics plays an important role in many signalling pathways [Rom+21; CWM21]. This phenomena is referred to as mechanotransduction which, broadly speaking, is any process by which cells convert mechanical stimuli into chemical signals [HDS14; SIC23].

A large number of recent works study the role of Rho GTPases, primarily RhoA, in mechanotransduction in relation to different mechanical cues: extracellular matrix (ECM) stiffness and viscoelasticity, tensile stress (stretching), compression (compressive stress), and shear stress (fluid flow shear), see e.g. [BMG19; Xie+23] for a review. Moreover, the coupling between biochemistry and mechanics is bidirectional, i.e., chemical signals can also affect the mechanical properties of the cell, such as molecules like focal adhesion kinases (FAKs) that influence F-actin dynamics and therefore the stiffness of the cell [Mar+18; SIC23; SGF16; YR23].

The formidable complexity of the phenomena involved in mechanotransduction means that much about how the mechanics and the chemical processes of the cell communicate is not yet understood and mathematical modelling is crucial in this regard. Whilst the mathematical modelling of biochemical cell signalling processes is fairly well developed, e.g., [Gil+06; GJG14; PV20], the study of mechanotransduction is comparatively more recent, see [Che+17] for a review. Typically the modelling involves solving coupled systems of partial differential equations (PDEs) with reaction-diffusion equations modelling the biochemistry coupled to equations based on (visco)elastic constitutive laws for the mechanics. The progress of such efforts has been rapid, ranging from early models employing simplifications such as one-dimensional geometries [BS07; Nov+21] to full three-dimensional simulations [SFR21] using advanced computational techniques. Alongside continuum models, a number of recent works have employed discrete approaches such as spring-based models [Kan+15], or models that employ a Potts formalism [Bar+99; Via+10; AS14]. Despite this rapid progress, the existing models typically make major simplifying assumptions such as assuming a constant stiffness of the ECM [SFR21; SSZ16; Ero+21], as well as neglecting the two-way coupling in which signalling pathways affect the mechanics alongside mechanical cues inducing signalling processes.

In the present work, we seek to develop, analyse and simulate a model for mechanotransduction through the Rho GTPase signalling pathway which allows for a two-way coupling between the mechanics and the biochemistry. The dynamics of the signalling molecules FAK and RhoA are modelled using reaction-diffusion equations, where the ECM stiffness and elastic stresses of the cell activate FAK. Under simplifying assumptions, i.e., assuming no dependence on the cell elastic stresses, the biochemical component of the model is derived as a reduction of the model proposed in [SFR21]. For the cell's mechanical properties, we assume an elastic constitutive relationship [Gou13] and

allow the material properties to depend on the concentrations of the signalling molecules. We propose a numerical method based on bulk and surface finite elements [DE13] for the approximation of the model equations.

The results presented here show that our model can reproduce the qualitative results of [SFR21], i.e., the mass of activated FAK and RhoA depend on ECM stiffness, with the dependence captured well by a Hill function. On the inclusion of the two-way coupling between signalling processes and cell mechanics, we observe novel dynamics, such as the conservation of cell deformation under different values of the ECM stiffness, which underlines the importance of including these more complex models of the mechanics. The role of mechanotransduction in homeostasis has been discussed in a number of biological works, e.g., [HDS14; CWM21; GW17; Mar+18; SGF16] and our work presents a concrete example of how modelling can help elucidate potential mechanisms that underlay the mechanical homeostasis. Homeostasis of cell deformation, as observed in simulations of our model, has been observed experimentally [Gro+23]. Our focus is on elastic constitutive assumptions for the mechanics of the cell to enhance clarity of exposition and to avoid unnecessary technical complexities. This can be extended to allow for other constitutive laws such as viscoelasticity of the cell and/or of the ECM as has been done elsewhere in the literature in simpler settings in 1D [BS07; MDS25]. This work thus serves as a starting point in modelling and analysis of the two-way coupling between mechanics and chemistry.

The paper is organised as follows. In Section 2 we derive the reduced model for the Rho GTPase signalling pathway, based on the model proposed in [SFR21]. In Section 3 the mathematical model for the mechanotransduction related to the Rho GTPase signalling pathway is derived. Simulations of the model are presented in Section 4. We conclude the paper with a discussion of the results in Section 5. Details on the numerical method applied to simulate the model equations are given in Appendix A.3.

## 2 A Mathematical model for the Rho GTPase signalling pathway

One of the main signaling pathways involved in mechanotransduction is the Rho GTPase pathway, responsible for many important cellular processes, e.g. motility, cell adhesion, polarisation, differentiation, remodelling of the exoskeleton, and the ECM [Xie+23]. The RhoA signalling pathway is activated through the activation of FAK in response to tension on integrins, which depends on ECM stiffness [Tom+09; YR23].

Our model for mechanotransduction related to the RhoA-mediated intercellular signalling pathway is based on models developed in [SFR21] and [Ero+21; SSZ16]. To incorporate the interactions between mechanics and signalling processes, we extend the model proposed in [SFR21] by considering elastic deformations of the cell. Activated FAK is downstream in the RhoA GTPase signalling pathway and hence the activation of RhoA is a function of activated FAK. The activation of RhoA results in ECM remodelling and deposition of new fibres, increasing ECM stiffness and hence activation of FAK [Di+23]. FAK is expressed in the cytoplasm of the cell and is activated on the cell membrane. To simplify the model and focus only on the most significant aspects from the perspective of qualitative behaviour, we reduce the model for the RhoA signalling pathway of [SFR21] that includes the dynamics of FAK, RhoA, ROCK, Myo, LIMK, mDia, Cofilin, F-actin and YAP/TAZ by considering only the dynamics of FAK and activated RhoA. Such a reduction is possible since other molecules considered in the full model of [SFR21] do not influence the dynamics of FAK and RhoA. Our rationale behind considering a simplified model is to more clearly elucidate the emergent features that arise when mechanics is coupled with signalling. It is not challenging to incorporate other biochemical species or different reaction kinetics within the framework we propose.

We let  $Y \subset \mathbb{R}^N$ ,  $N = 2, 3$ , denote the cytoplasm and  $\Gamma = \partial Y$  the cell membrane. We denote by  $\phi_d$  and  $\phi_a$  the concentrations of inactive and active FAK, and by  $\rho_a$  the concentration of active RhoA. We recall that inactive species are assumed to be cytoplasm resident and activated forms membrane resident. Our reduced model for the biochemistry consists of the following system of reaction-diffusion equations

$$\begin{aligned}
\partial_t \phi_d - D_1 \Delta \phi_d &= k_1 \phi_a && \text{in } Y, t > 0, \\
\partial_t \phi_a - D_2 \Delta \phi_a &= -k_1 \phi_a && \text{in } Y, t > 0, \\
D_1 \nabla \phi_d \cdot \nu &= -k_2 \phi_d - k_3 \frac{E}{C + E} \phi_d && \text{on } \Gamma, t > 0, \\
D_2 \nabla \phi_a \cdot \nu &= k_2 \phi_d + k_3 \frac{E}{C + E} \phi_d && \text{on } \Gamma, t > 0, \\
\partial_t \rho_a - D_3 \Delta_\Gamma \rho_a &= -k_4 \rho_a + k_5 (\hat{\gamma}(\phi_a)^n + 1) \left( \rho_d^0 - \frac{(\rho_a - \rho_a^0)}{n_r} \right) && \text{on } \Gamma, t > 0,
\end{aligned} \tag{1}$$

where  $\rho_d^0 - \frac{(\rho_a - \rho_a^0)}{n_r}$  is an approximation for deactivated RhoA ( $\rho_d$ ) on the surface,  $\Delta_\Gamma$  is the Laplace Beltrami

operator modelling diffusion on the surface  $\Gamma$ , see e.g. [DE13],  $n_r = |Y|/|\Gamma|$  is the ratio between the volume of the cytoplasm and the area of the cell membrane,  $k_1, k_4$  are deactivation and  $k_2, k_3, k_5$  are activation constants,  $E$  is the substrate stiffness,  $D_1, D_2, D_3$  are the diffusion constants,  $C, n$  and  $\hat{\gamma}$  are positive constants, and  $\rho_d^0$  and  $\rho_a^0$  are the initial concentrations of deactivated and activated RhoA. Simulations illustrating the agreement between results obtained using the reduced model (1) with those of [SFR21] for the full model are presented in Appendix A.1.

### 3 Mathematical model for mechanotransduction

As a starting point for the mechanics, we consider small deformations and hence, assume a linear elastic constitutive law for the mechanics of the cell. Although viscoelastic or poroelastic behaviour of cells is proposed in many works [Kas+07; Moe+13], linear elasticity is often chosen for modelling simplicity as it can yield results consistent with experimental observations [BM13; Oak+14; CSZ20]. An important simplification that arises under the small deformations assumption is that the model for the biochemistry (1) remains consistent without additional terms depending on the material velocity of the cell. If the assumption of small deformations is relaxed, the coupled model is considerably more complicated and will be addressed in future studies. The cell nucleus plays an important role in governing the mechanical properties of the cell [GB16], whilst we predominantly neglect this in the present work, in Appendix A.5 we have included simulations of a ‘passive’ nucleus that is modelled to be more rigid than the cytoplasm.

It has been shown that the stiffness of the cell increases as F-actin increases [SFR21]. Since in the reduced model, we do not consider the dynamics of F-actin explicitly, we use activated FAK as a proxy for F-actin and assume that the Young’s modulus  $E_c$  of the cell is a function of the activated FAK concentration. Based on experimental observations [Gar+04] and numerical simulations [SFR21], we propose

$$E_c = E_c(\phi_a) = k_7(k_8 + \phi_a^p), \quad (2)$$

where  $k_7, k_8$  and  $p$  are non-negative constants. Then for elastic deformations of the cell, we have

$$-\nabla \cdot \sigma(u) = 0 \quad \text{in } Y, \quad (3)$$

with

$$\sigma(u) = \lambda(\phi_a)(\nabla \cdot u)I + \mu(\phi_a)(\nabla u + (\nabla u)^T)$$

and the Lamé constants  $\lambda$  and  $\mu$  are given by

$$\lambda(\phi_a) = \frac{E_c(\phi_a)\nu_c}{(1 + \nu_c)(1 - 2\nu_c)}, \quad \mu(\phi_a) = \frac{E_c(\phi_a)}{2(1 + \nu_c)},$$

where  $\nu_c$  is the Poisson ratio of the cell.

Activated RhoA regulates remodelling of stress fibres inside the cell and stabilisation of actin filaments [BG16; Doy+15; Zha+07; CB96]. This mechanism is modelled by the stress on the boundary being dependent on activated RhoA concentration

$$\sigma(u) \cdot \nu = \mathbb{P}(k_6 \rho_a \nu) \quad \text{on } \Gamma, \quad (4)$$

where  $k_6$  is a positive constant,  $\mathbb{P}$  is a projection on the space orthogonal to the space of rigid deformations, i.e. rotations and translations. Alongside models where the cell is allowed to deform freely, to model a typical experimental set-up where cells are placed on a rigid substrate, we consider

$$u \cdot \nu = 0, \quad \Pi_\tau(\sigma(u) \cdot \nu) = 0 \quad \text{on } \Gamma_0, \quad (5)$$

together with condition (4) on  $\Gamma \setminus \Gamma_0$ , where  $u_3$  is the deformation in the vertical  $x_3$ -direction,  $\Pi_\tau(w) = w - (w \cdot \nu)\nu$  denotes the tangential projection of vector  $w$ , and  $\Gamma_0 = \Gamma \cap \{x \in \mathbb{R}^3 | x_3 = 0\}$ .

It has been shown that an increased contractility is associated with increased activated FAK, see e.g. [BG16]. Thus we assume that FAK is activated by the stress of the cell and as a proxy for the cytosolic stress we use the positive part of trace of the Cauchy stress tensor  $\text{tr}(\sigma)_+$ , where  $\text{tr}(\sigma)$  is the first stress invariant and the positive part reflects the fact that extension rather than compression causes the activation of FAK. This modifies system

(1) to

$$\begin{aligned}
\partial_t \phi_d - D_1 \Delta \phi_d &= k_1 \phi_a - C_1 \text{tr}(\sigma)_+ \phi_d && \text{in } Y, t > 0, \\
\partial_t \phi_a - D_2 \Delta \phi_a &= -k_1 \phi_a + C_1 \text{tr}(\sigma)_+ \phi_d && \text{in } Y, t > 0, \\
D_1 \nabla \phi_d \cdot \nu &= -k_2 \phi_d - k_3 \frac{E}{C + E} \phi_d && \text{on } \Gamma, t > 0, \\
D_2 \nabla \phi_a \cdot \nu &= k_2 \phi_d + k_3 \frac{E}{C + E} \phi_d && \text{on } \Gamma, t > 0, \\
\partial_t \rho_a - D_3 \Delta \Gamma \rho_a &= -k_4 \rho_a + k_5 (\hat{\gamma}(\phi_a)^n + 1) \left( \rho_d^0 - \frac{(\rho_a - \rho_a^0)}{n_r} \right) && \text{on } \Gamma, t > 0,
\end{aligned} \tag{6}$$

where  $v_+ = \max\{v, 0\}$ . We can prove existence, uniqueness and boundedness of solutions to system (3)-(6) which we intend to report on elsewhere.

## 4 The interplay between signalling and mechanics: simulation results

Using model (3)-(6) we investigate different scenarios demonstrating the interactions between mechanics and signalling processes. First, we consider the impact of the cell Young's modulus  $E_c$  and compare the dynamics when considering a constant  $E_c$  versus the case where  $E_c$  depends on activated FAK as defined in (2). We also model the effect of the stress on the signalling molecules FAK and simulate equations (6) for  $C_1 = 0$  and  $C_1 = 1$ , respectively. Additionally we consider two experimental scenarios: (i) the cell is placed on a rigid substrate, modelled by the boundary conditions (4) on  $\Gamma \setminus \Gamma_0$  and (5) on  $\Gamma_0$  or (ii) the cell is embedded in an agar and only the force boundary condition (4) on the entire cell membrane is considered. We also distinguish between two different stimuli, similar to [SFR21], (i) the so called '2xD stimulus', where the substrate stiffness is only applied to the bottom of the cell, i.e.  $E$  is nonzero only on  $\Gamma_0$ , and (ii) the '3D stimulus' where the cell is embedded in an agar (substrate) and the impact of the substrate stiffness on the signalling processes is considered on the whole cell membrane. To analyse the impact of the cell shape on the dynamics of signalling molecules and mechanical deformations we consider both radially symmetric cells and polarised cells with a lamellipodium like structure. The distance between the base at the nucleus to the rear of the cell is larger for the lamellipodium cells such that the volume is similar to the radially symmetric cells.

The parameters in the reaction-diffusion equations are chosen as in Table 1, and the parameters in the elasticity equations are specified in Table 2. For numerical simulations, we use a Finite Element Method to discretize in space and a semi-implicit Euler method to discretize in time, with the mesh size  $h = 2.94 \mu\text{m}$  and time step  $dt = 0.5 \text{ s}$ . Details on the numerical approach and benchmark computations demonstrating the accuracy of the approach for a problem with a known solution are given in Appendix A.3.

$\phi_d^0 = 0.7 \mu\text{M}$	$C = 3.25 \text{ kPa}$	$D_1 = 4 \mu\text{m}^2/\text{s}$	$k_2 = 0.015 \frac{[Y]}{[\Gamma]} \text{ s}^{-1}$
$\phi_a^0 = 0.3 \mu\text{M}$	$\gamma = 77.56 \mu\text{M}^{-5}$	$D_2 = 4 \mu\text{m}^2/\text{s}$	$k_3 = 0.379 \frac{[Y]}{[\Gamma]} \text{ s}^{-1}$
$\rho_a^0 = 33.6 \#/\mu\text{m}^2$	$n = 5$	$D_3 = 0.3 \mu\text{m}^2/\text{s}$	$k_4 = 0.625 \text{ s}^{-1}$
$C_1 = 0 \text{ or } 1$	$E = 0.1, 5.7, 7 \cdot 10^6 \text{ kPa}$	$k_1 = 0.035 \text{ s}^{-1}$	$k_5 = 0.0168 \frac{[Y]}{[\Gamma]} \text{ s}^{-1}$

Table 1: Parameter values for simulations of model (6).

$v_c$	$0.3 - 0.5$	$0.3$
$k_6 (\text{s}^{-1})$	$0.1 - 2$	$1$
$k_7 (\text{s}^{-1})$	$2 - 3$ [SFR21]	$2$
$k_8 (\text{s}^{-1})$	$0.01 - 0.5$ [SFR21]	$0.1$
$p$	$2 - 3$ [Gar+04; SFR21]	$2.6$

Table 2: Parameters for simulations of model (3)-(5).

### 4.1 Simulations with 2xD stimulus

First we look at the results that would most reflect a cell on a substrate in vitro. Here, the substrate stiffness appears as a stimulus only on the bottom boundary of the cell, i.e.  $E$  is nonzero only on  $\Gamma_0$ , and deformation is

restricted in the vertical direction at the bottom boundary of the cell. The results for the radially symmetric shape of the cell are found in Figure 1, whereas results for the lamellipodium shape are presented in Figure 3. Note that results for  $\phi_a$  and  $\rho_a$  when  $E_c = 0.6$  and  $C_1 = 0$  are identical to the one without mechanics in Figure A1, Appendix A. In this case, we see that the deformation  $u$  is largest at the edge of the cell. The cell expands radially symmetrically at the base. As expected, the expansion is larger for higher concentrations of  $\phi_a$ . For a lower substrate stiffness,  $E = 0.1\text{kPa}$ , the cell barely expands. When  $C_1 = 1$ , the concentrations of  $\phi_a$  and  $\rho_a$  and the magnitude of the deformation  $|u|$  increase, with a bigger increase for lower substrate stiffness and a smaller increase for larger substrate stiffness. When comparing  $E_c = 0.6$  and  $E_c = f(\phi_a)$ , the deformations show similar patterns, expanding at the base of the cell, however, the magnitude of the deformation is much lower in the case  $E_c = f(\phi_a)$ . This is probably because  $E_c = f(\phi_a) \approx 0.6$  for a small substrate stiffness  $E$ , but is doubled in magnitude for larger substrate stiffness, see Figure 5. The larger cell Young's modulus  $E_c$  means it is harder for the cell to deform, resulting in a lower magnitude of deformation. This difference illustrates that, unlike the constant Young's modulus case, a concentration-dependent Young's modulus allows for potential homeostasis and adaptation of cell mechanics to different values of the substrate stiffness [Gro+23].

For the two-way couplings between the mechanics and chemistry, i.e.  $E_c = f(\phi_a)$  and  $C_1 = 1$ , we see similar results for the deformation as when  $E_c = f(\phi_a)$  and  $C_1 = 0$ . The main difference is that the deformation for  $E = 0.1\text{ kPa}$  is now at a similar magnitude as for the larger substrate stiffnesses, demonstrating the importance of the signalling processes in the adaptation of cell mechanics to changing environmental conditions.

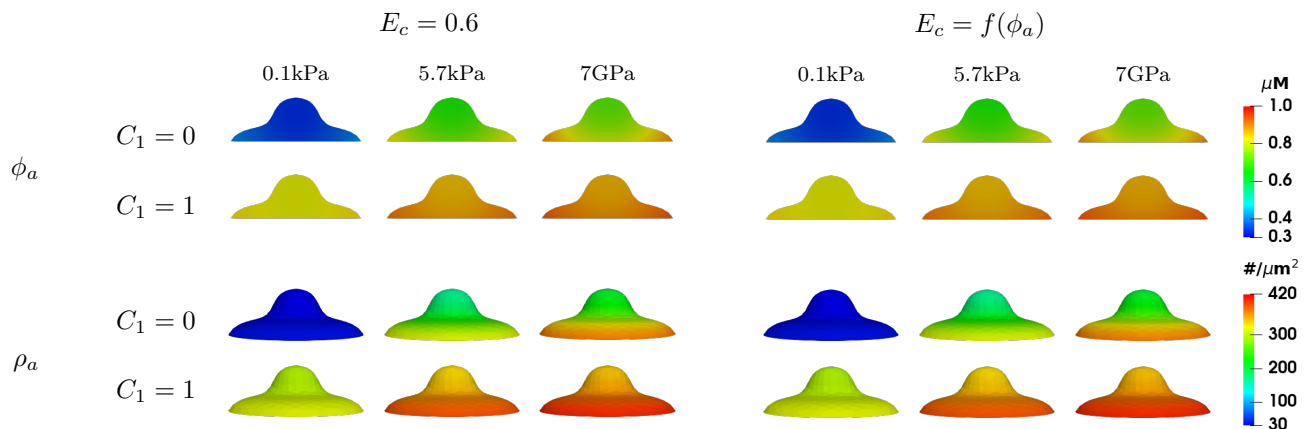


Figure 1: Numerical simulation results of section 4.1 showing  $\phi_a$  and  $\rho_a$  for model (3)-(6) for radially symmetric cells at steady state for  $T = 100\text{ s}$ . Four different scenarios corresponding to  $C_1 = 0$  and  $C_1 = 1$ , and  $E_c = 0.6$  and  $E_c = f(\phi_a)$  are considered. Within each figure, the rows are  $\phi_a$  and  $\rho_a$ , and the columns are  $E = 0.1, 5.7, 7 \cdot 10^6\text{ kPa}$ . Parameter values as in Tables 1 and 2.

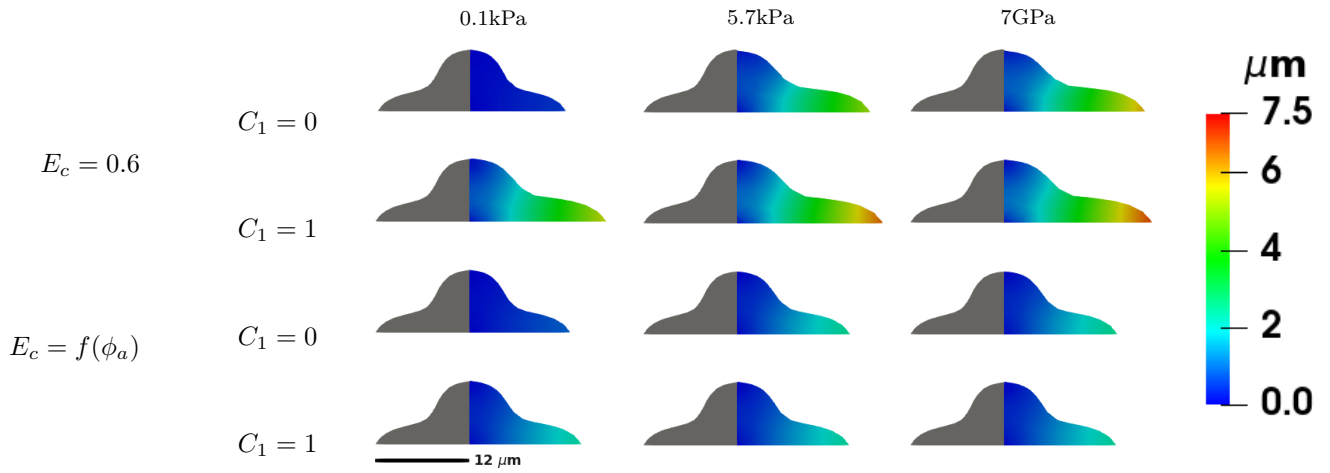


Figure 2: Numerical simulation results of section 4.1 showing  $u$  for model (3)-(6), for radially symmetric cells at steady state for  $T = 100$  s. Four different scenarios corresponding to  $C_1 = 0$  and  $C_1 = 1$ , and  $E_c = 0.6$  and  $E_c = f(\phi_a)$  are considered. Within each figure the columns are  $E = 0.1, 5.7, 7 \cdot 10^6$  kPa. Parameter values as in Tables 1 and 2.

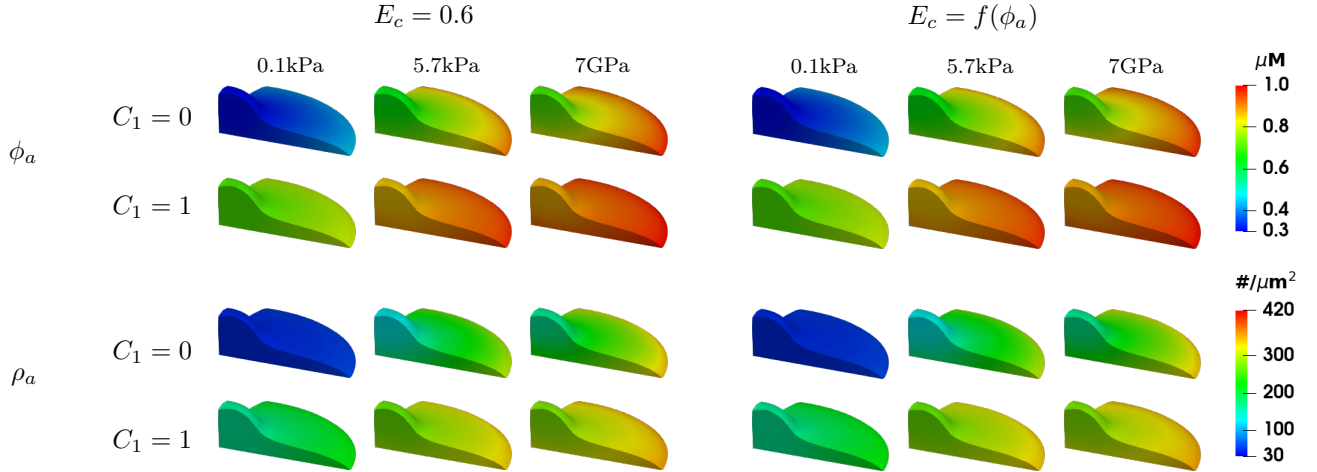


Figure 3: Numerical simulation results of section 4.1 showing showing  $\phi_a$  and  $\rho_a$  for model (3)-(6) for the lamellipodium shape cells at steady state for  $T = 100$  s. Four different scenario corresponding to  $C_1 = 0$  and  $C_1 = 1$ , and  $E_c = 0.6$  and  $E_c = f(\phi_a)$ . Within each figure, the rows are  $\phi_a$  and  $\rho_a$ , and the columns are  $E = 0.1, 5.7, 7 \cdot 10^6$  kPa. Parameter values as in Tables 1 and 2.

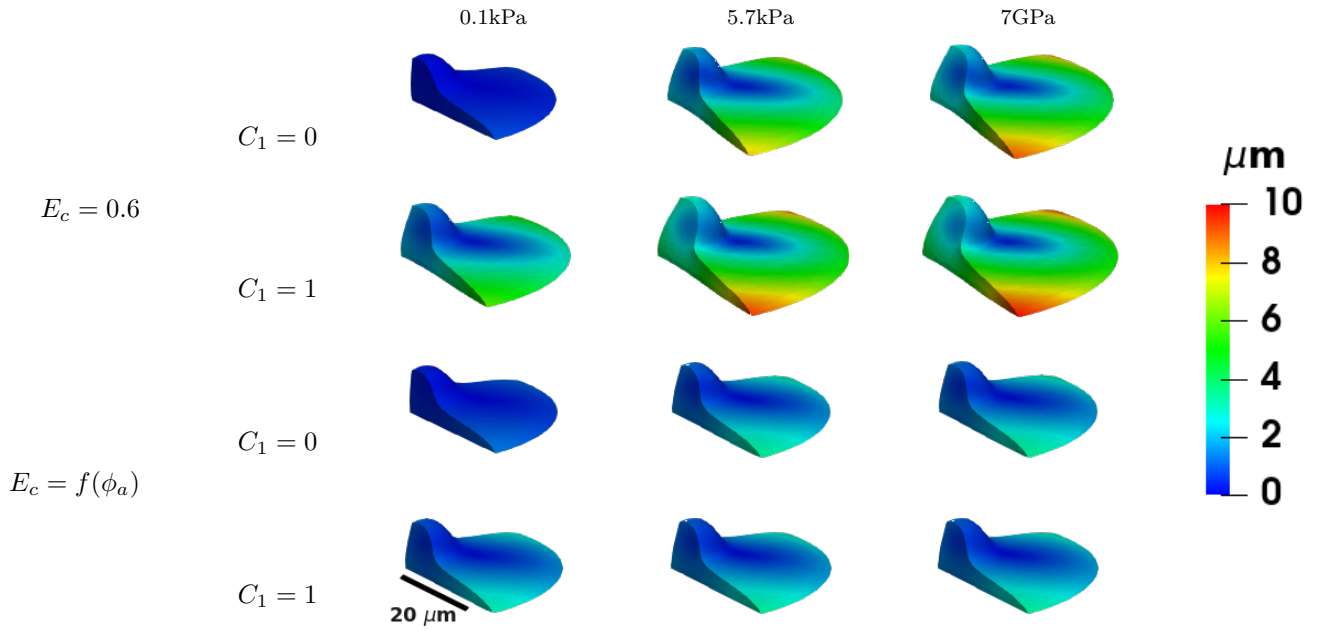


Figure 4: Numerical simulation results of section 4.1 showing  $u$  for model (3)-(6) for the lamellipodium shape cells at steady state for  $T = 100$  s. Four different scenario corresponding to  $C_1 = 0$  and  $C_1 = 1$ , and  $E_c = 0.6$  and  $E_c = f(\phi_a)$ . Within each figure the columns are  $E = 0.1, 5.7, 7 \cdot 10^6$  kPa. Parameter values as in Tables 1 and 2.

Comparing the simulation results for the two different shapes in Figures 1 and 3, the concentration of activated RhoA,  $\rho_a$ , is slightly lower for the lamellipodium shape. For the lamellipodium shape, we observe the largest deformations at the corners with no radial symmetry.

Figure 5 summarises the results at time  $T = 100$  s by plotting the mean,  $\frac{1}{|\Omega|} \int_{\Omega} \cdot dx$ , of  $E_c = f(\phi_a)$ ,  $\text{div}(u)$ ,  $\phi_a$ , and  $\rho_a$  as functions of the substrate stiffness  $E$  with the bars being the range of these variables for different values of the constant  $C_1$  in the activation of FAK by the cell stress. As expected, an increase in  $C_1$  results in an increase in the concentration of activated FAK  $\phi_a$ . The dependence of  $\phi_a$  on the substrate stiffness  $E$ , especially for  $C_1 = 0, 0.5$ , resembles a Hill function representing a threshold response. This agrees with simulations in [SFR21] which themselves fit experimental observations presented in [BCP17]. For most of the cases, the results for the lamellipodium shape are very similar to the results for the radially symmetric shape. However, for  $C_1 = 1$ , the magnitude of the threshold-like response in all variables is much bigger in the lamellipodium case due to smaller values for the lower  $E$  level. In terms of the Young's modulus when  $E_c = 0.6$  we observe much larger volume changes than when  $E_c = f(\phi_a)$  in all the numerical experiments.

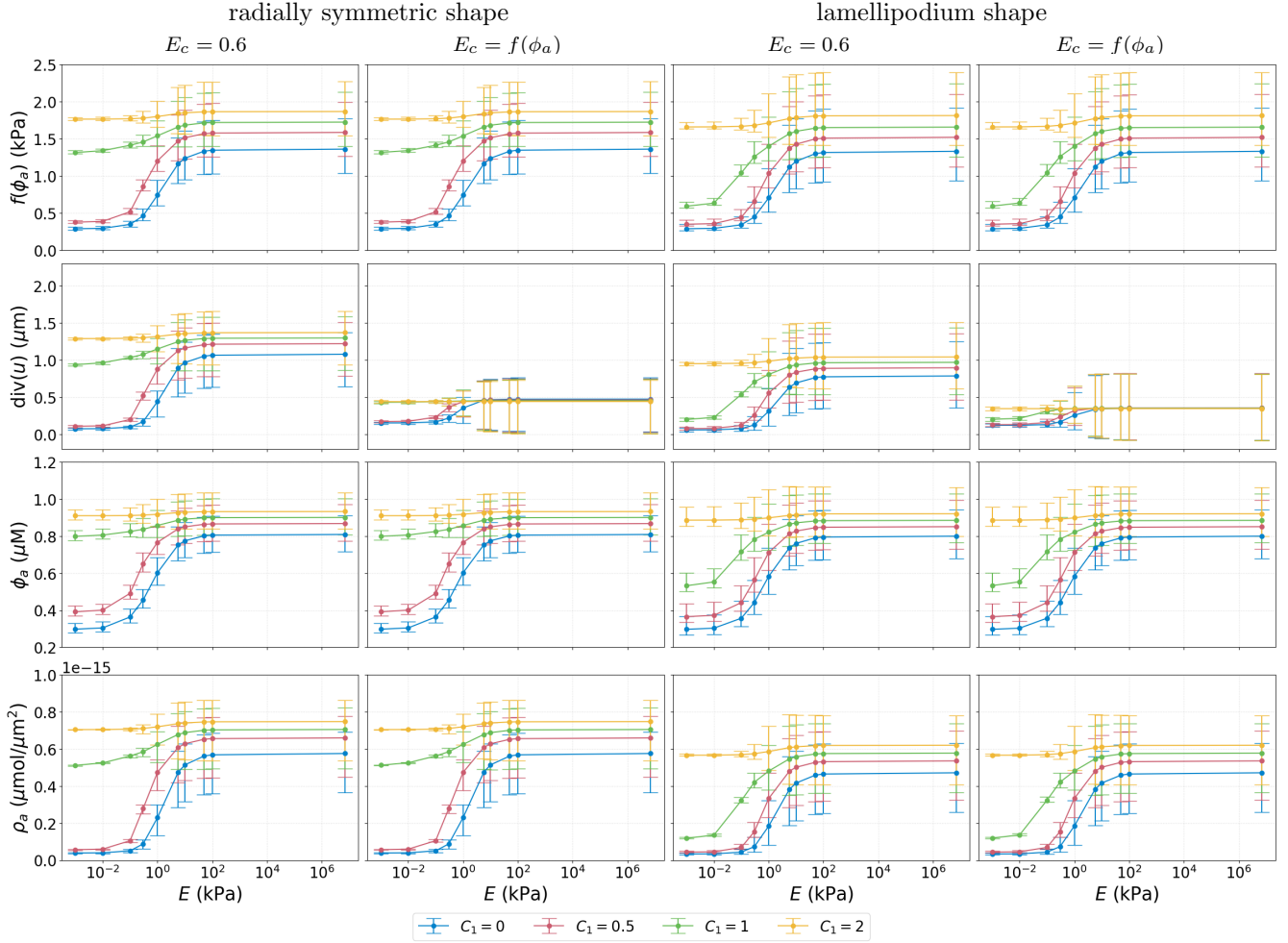


Figure 5: Simulation results of section 4.1 showing  $f(\phi_a)$ ,  $\text{div}(u)$ ,  $\phi_a$  and  $\rho_a$  as functions of substrate stiffness  $E$ , for different couplings with a range of values for  $C_1$  and two different shapes at steady state for  $T = 100$  s. All other parameter values as in Tables 1 and 2.

## 4.2 Numerical simulations for the 3D stimulus case on a rigid substrate

In numerical simulations for a 3D stimulus on a rigid substrate, the substrate stiffness affects the whole cell membrane and we consider the boundary conditions (4) on  $\Gamma \setminus \Gamma_0$  and (5) on  $\Gamma_0$ . The results for numerical experiments analogous to those of section 4.1 are reported in Figures 6–10. Overall, the concentrations  $\phi_a$  and  $\rho_a$  are larger than in the case of the 2xD stimulus, which is in line with the results in [SFR21]. The higher concentrations of  $\rho_a$  results in larger deformations, where the maximum deformation in the case of the 2xD stimulus was  $7 \mu\text{m}$ , see Figure 1, while the maximum deformation in the case of the 3D stimulus is  $7.5 \mu\text{m}$ , see Figure 6. Similar behaviour is observed for the lamellipodium shape, see Figures 3 and 8. Another difference between two cases are larger variations in concentration and a larger difference between maximal and minimal values in the case of the 2xD stimulus than in the case of 3D stimulus, see Figures 5 and 10. Similar behaviour is observed also in the model for the signalling processes without mechanics, see Figures A1 and A2 in the Appendix.



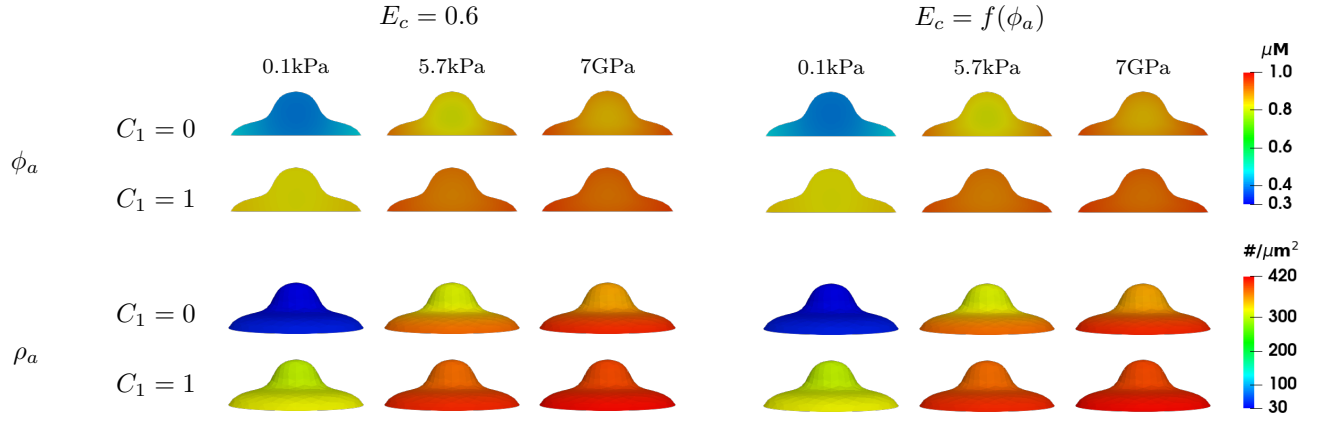


Figure 6: Numerical simulation results of section 4.2 showing  $\phi_a$  and  $\rho_a$  for model (3)-(6) for the radially symmetric shape and in the case of the 3D stimulus at steady state for  $T = 100$  s. Within each figure the columns are  $E = 0.1, 5.7, 7 \cdot 10^6$  kPa and parameter values as in Tables 1 and 2.

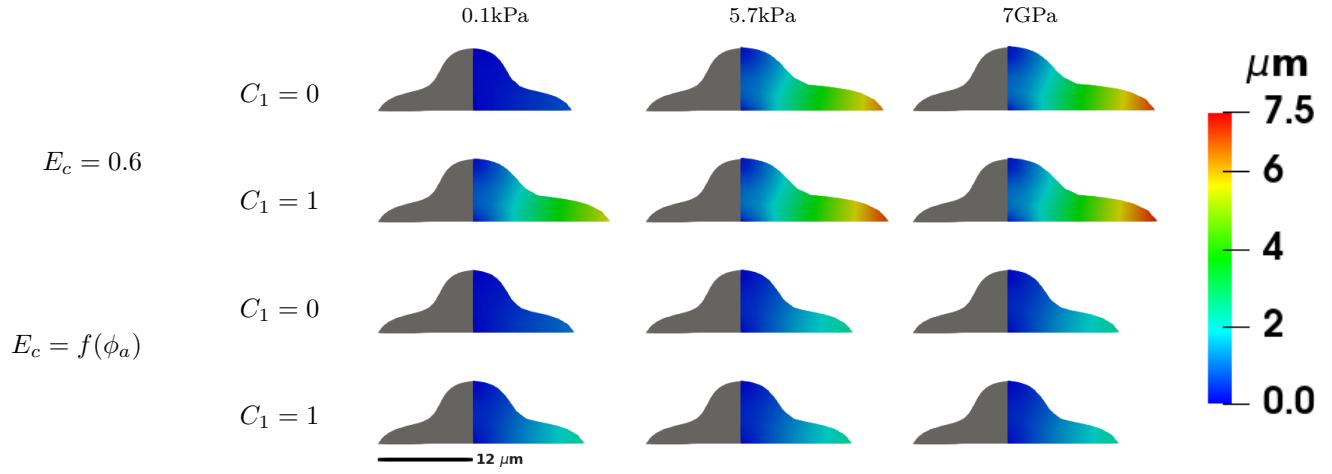


Figure 7: Numerical simulation results of section 4.2 showing  $u$  for model (3)-(6) for the radially symmetric shape and in the case of the 3D stimulus at steady state for  $T = 100$  s. Within each figure the columns are  $E = 0.1, 5.7, 7 \cdot 10^6$  kPa and parameter values as in Tables 1 and 2.

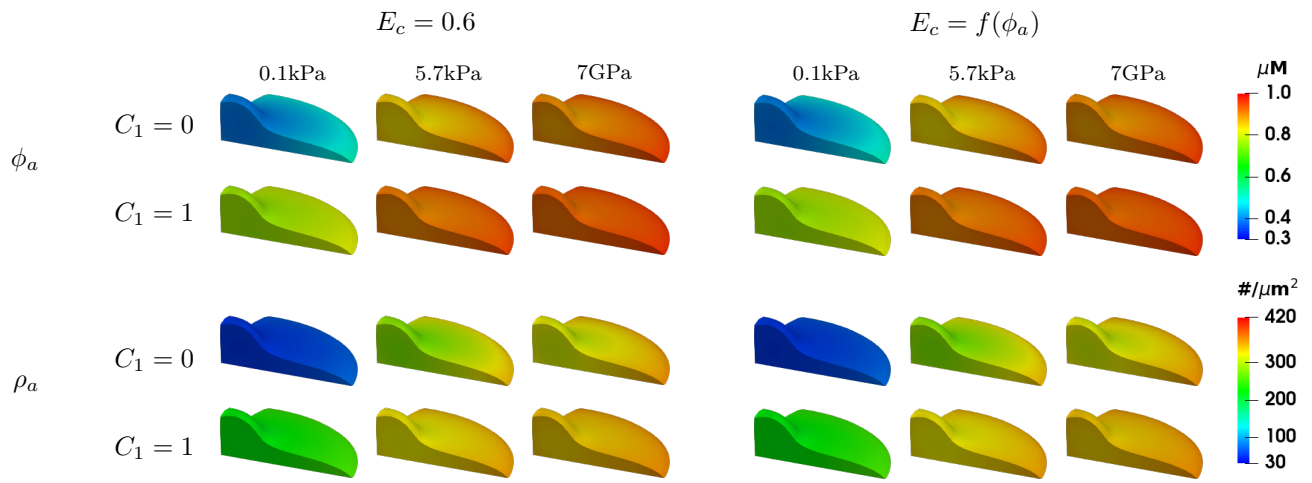


Figure 8: Numerical simulation results of section 4.2 showing  $\phi_a$  and  $\rho_a$  for model (3)-(6) for the lamellipodium shape and in the case of the 3D stimulus at steady state for  $T = 100$  s. Within each figure the columns are  $E = 0.1, 5.7, 7 \cdot 10^6$  kPa and parameter values as in Tables 1 and 2.

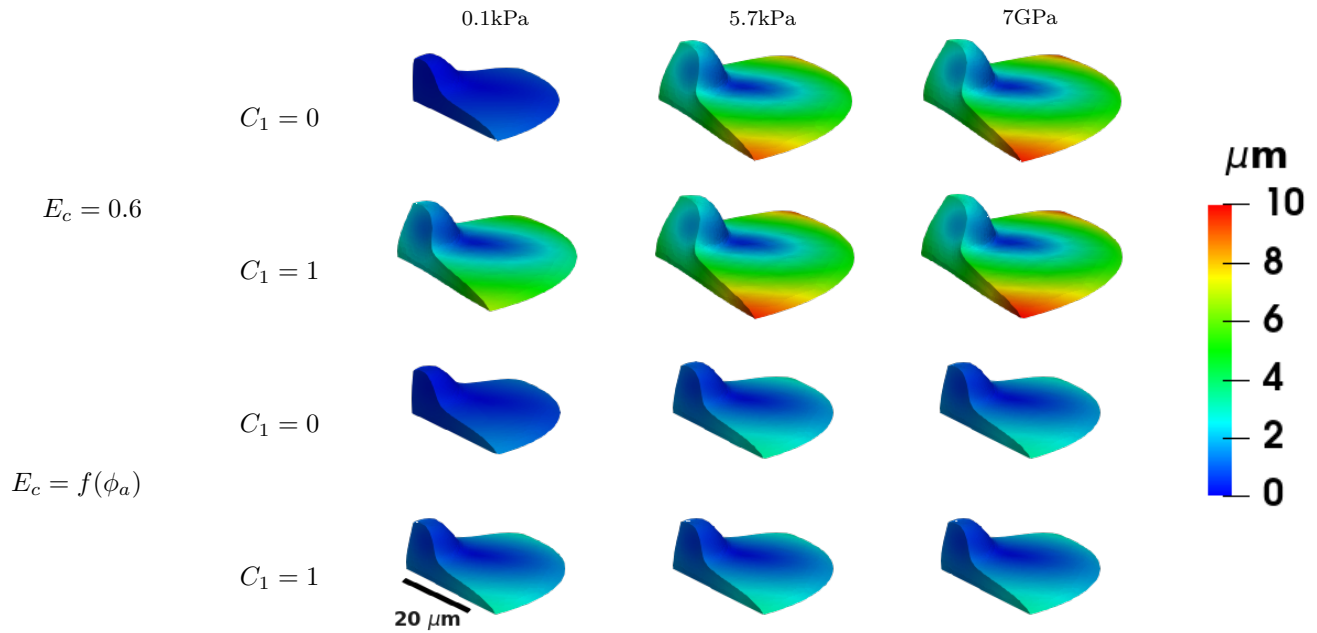


Figure 9: Numerical simulation results of section 4.2 showing  $u$  for model (3)-(6) for the lamellipodium shape and in the case of the 3D stimulus at steady state for  $T = 100$  s. Within each figure the columns are  $E = 0.1, 5.7, 7 \cdot 10^6$  kPa and parameter values as in Tables 1 and 2.

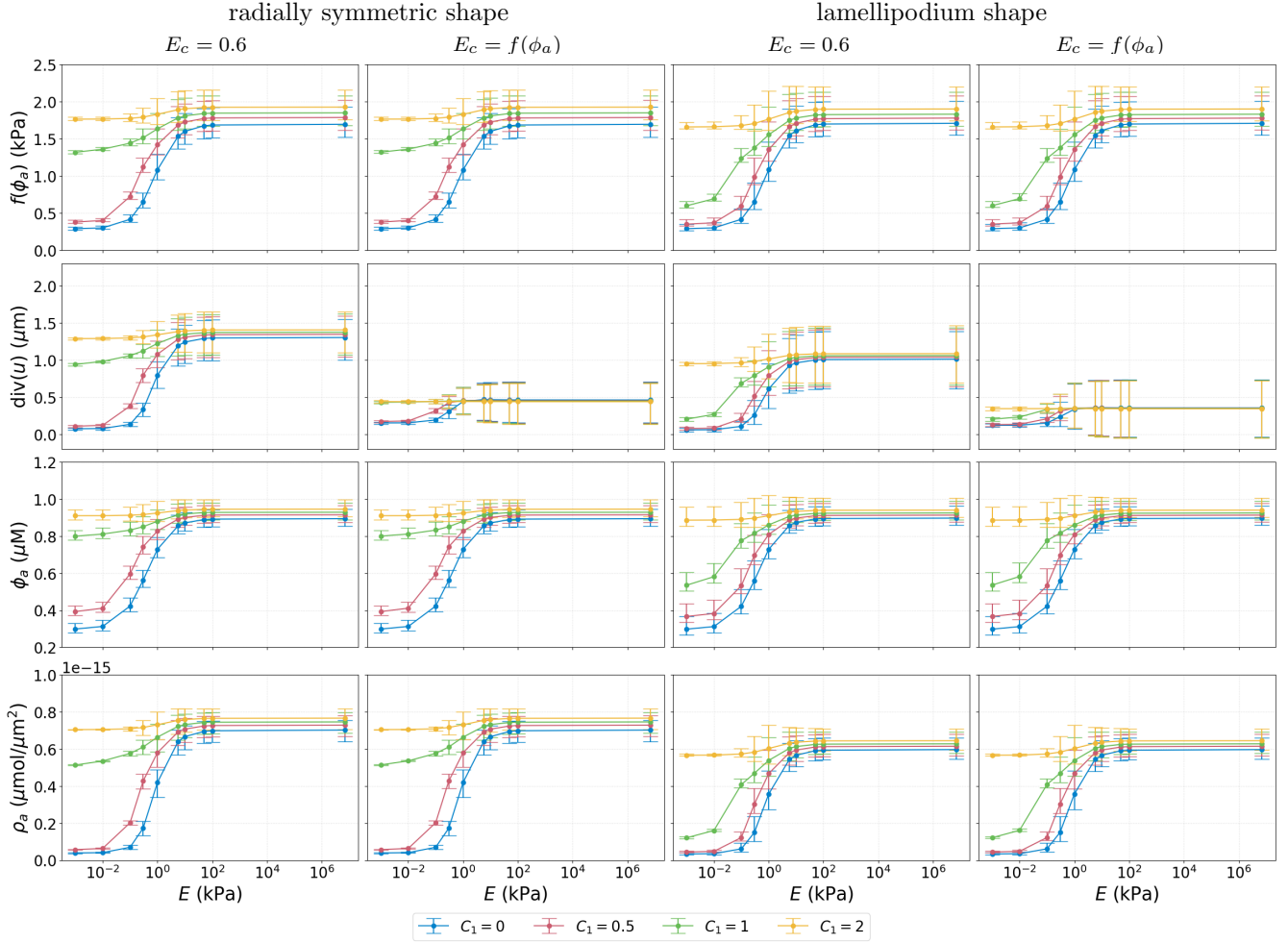


Figure 10: Simulation results of section 4.2 showing  $f(\phi_a)$ ,  $\text{div}(u)$ ,  $\phi_a$  and  $\rho_a$  as functions of substrate stiffness  $E$ , for different couplings with a range of values for  $C_1$  and two different shapes at steady state for  $T = 100$  s. All other parameter values as in Tables 1 and 2.

### 4.3 Numerical simulations for model (3), (4), and (6).

To investigate a setting more close to a cell in vivo, we consider the coupled model (3)-(4), (6) with force boundary conditions on the whole cell membrane, without restricting the deformation on the bottom of the cell.

#### 4.3.1 Numerical simulations in the case of 3D stimulus.

Simulation results for a 3D stimulus that models a cell surrounded by the extracellular matrix are presented in Figures 11-15. The results show the same differences between the different couplings as in section 4.2. Comparing Figures 6 and 11, the results for the concentrations  $\phi_a$  and  $\rho_a$  are indistinguishable, however there is a clear difference in deformation of the bottom of the cell and in the case of the fixed vertical deformations the deformation at the base of the cell is slightly lower than in the case of force boundary conditions. The same differences are observed for the lamellipodium shape case, see Figures 8 and 13. Comparing Figures 10 and 15, the main difference is in behaviour of  $\text{div}(u)$  as function of  $E$ . Even though the average volume change is the same, we see differences in the maximum and minimum values of the deformation across the domain. In particular, the maximum deformation when consider the model with a partially fixed boundary is larger and is located on the base of the cell, while the maximum deformation when consider the model with the force boundary conditions is smaller, but the cell deforms more evenly in all directions.

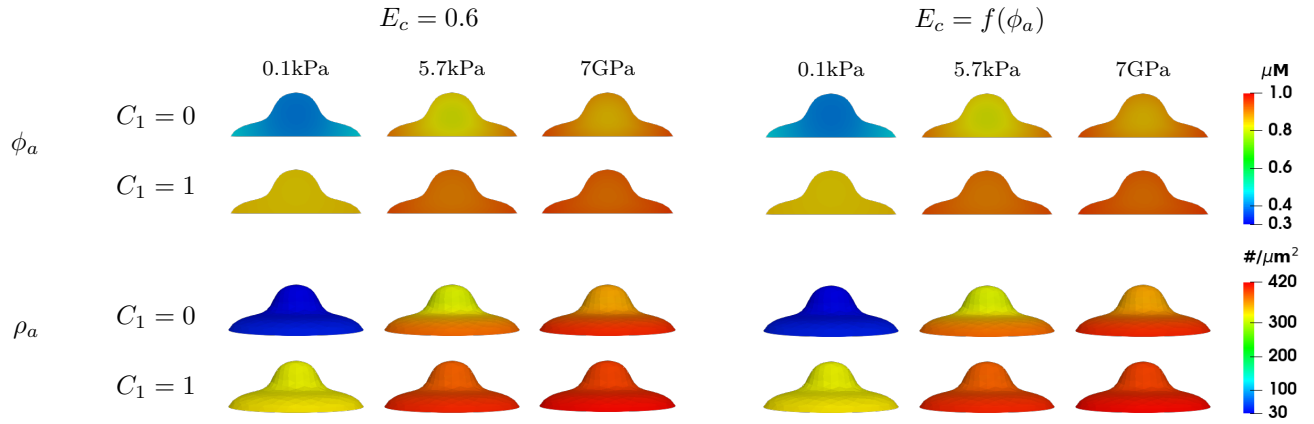


Figure 11: Numerical simulation results of section 4.3.1 showing  $\phi_a$  and  $\rho_a$  for model (3), (4), and (6) for the radially symmetric shape and in the case of the 3D stimulus at steady state for  $T = 100$  s. Within each figure the columns are  $E = 0.1, 5.7, 7 \cdot 10^6$  kPa and parameter values as in Tables 1 and 2.

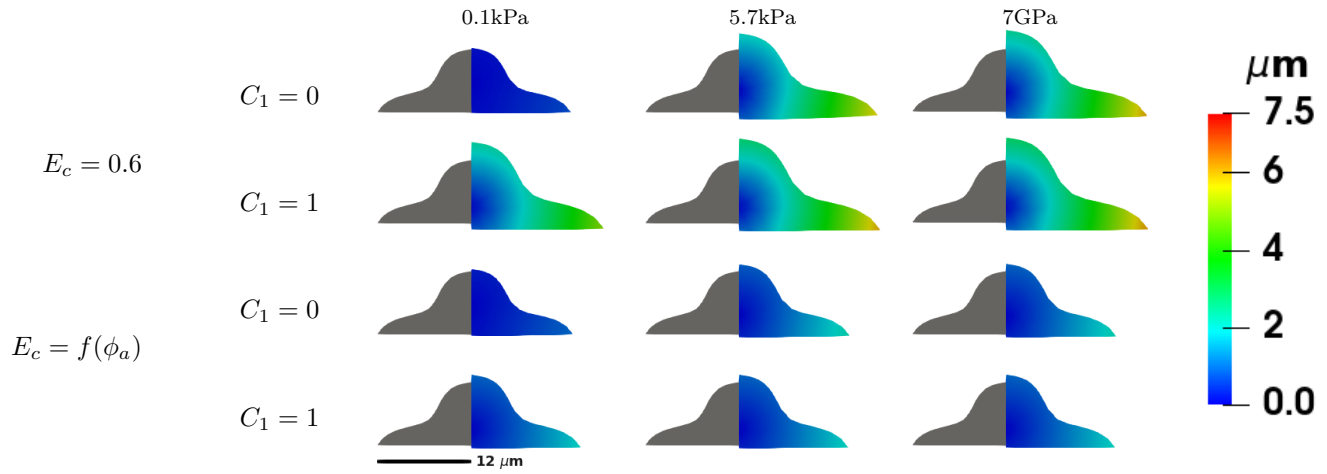


Figure 12: Numerical simulation results of section 4.3.1 showing  $u$  for model (3), (4), and (6) for the radially symmetric shape and in the case of the 3D stimulus at steady state for  $T = 100$  s. Within each figure the columns are  $E = 0.1, 5.7, 7 \cdot 10^6$  kPa and parameter values as in Tables 1 and 2.

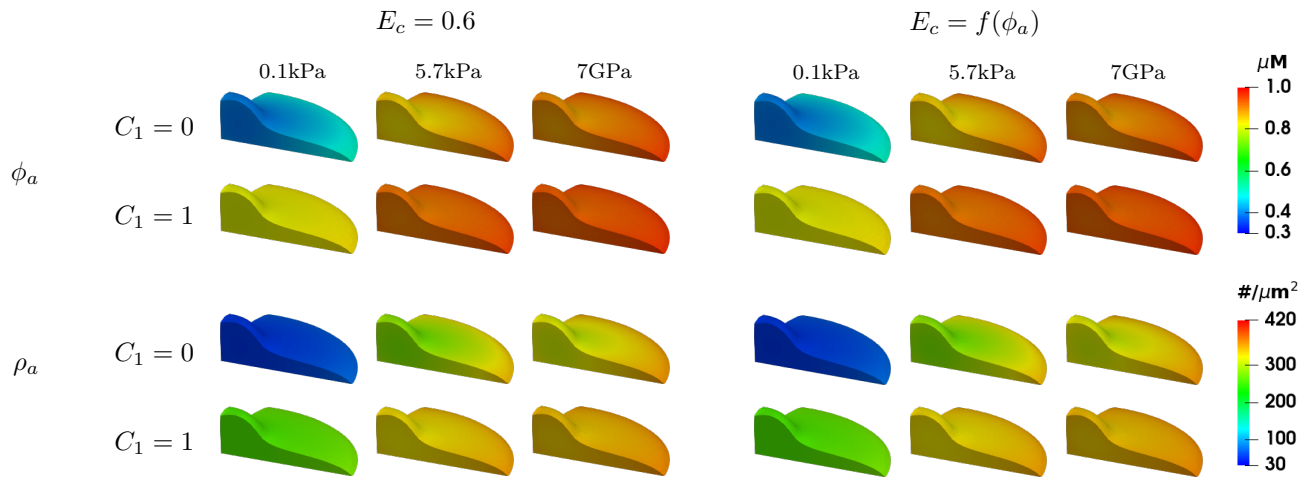


Figure 13: Numerical simulation results of section 4.3.1 showing  $\phi_a$  and  $\rho_a$  for model (3), (4), and (6) for the lamellipodium shape and in the case of the 3D stimulus at steady state for  $T = 100$  s. Within each figure the columns are  $E = 0.1, 5.7, 7 \cdot 10^6$  kPa and parameter values as in Tables 1 and 2.

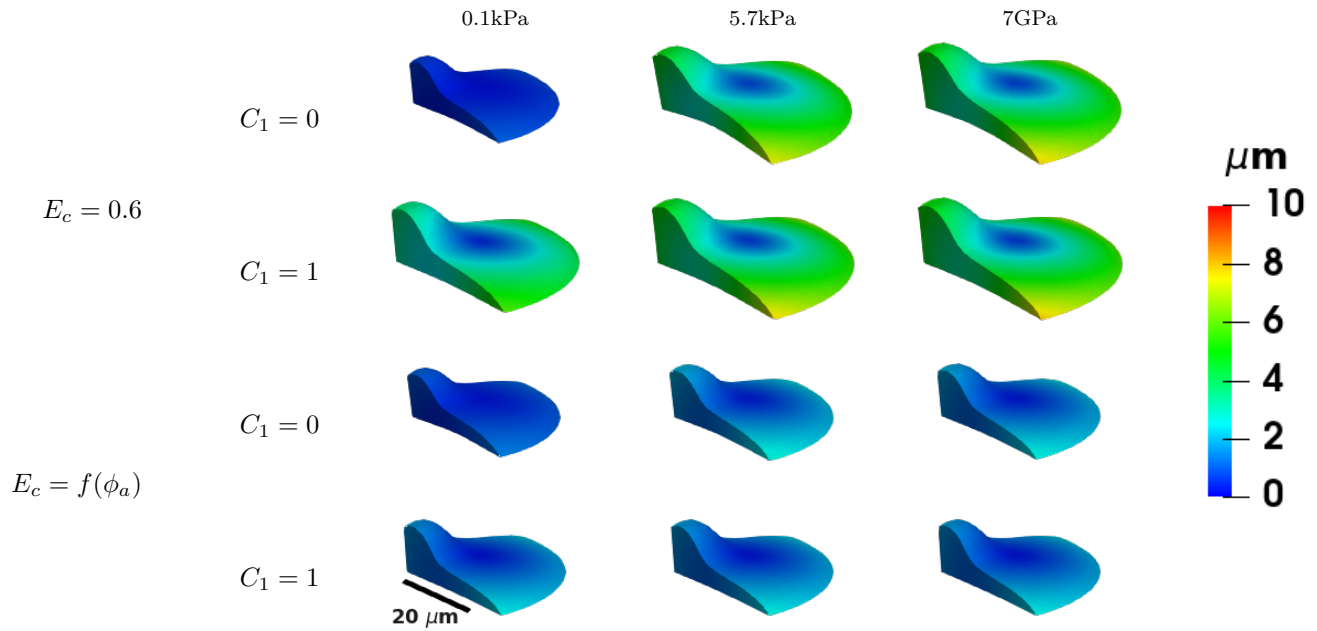


Figure 14: Numerical simulation results of section 4.3.1 showing  $u$  for model (3), (4), and (6) for the lamellipodium shape and in the case of the 3D stimulus at steady state for  $T = 100$  s. Within each figure the columns are  $E = 0.1, 5.7, 7 \cdot 10^6$  kPa and parameter values as in Tables 1 and 2.

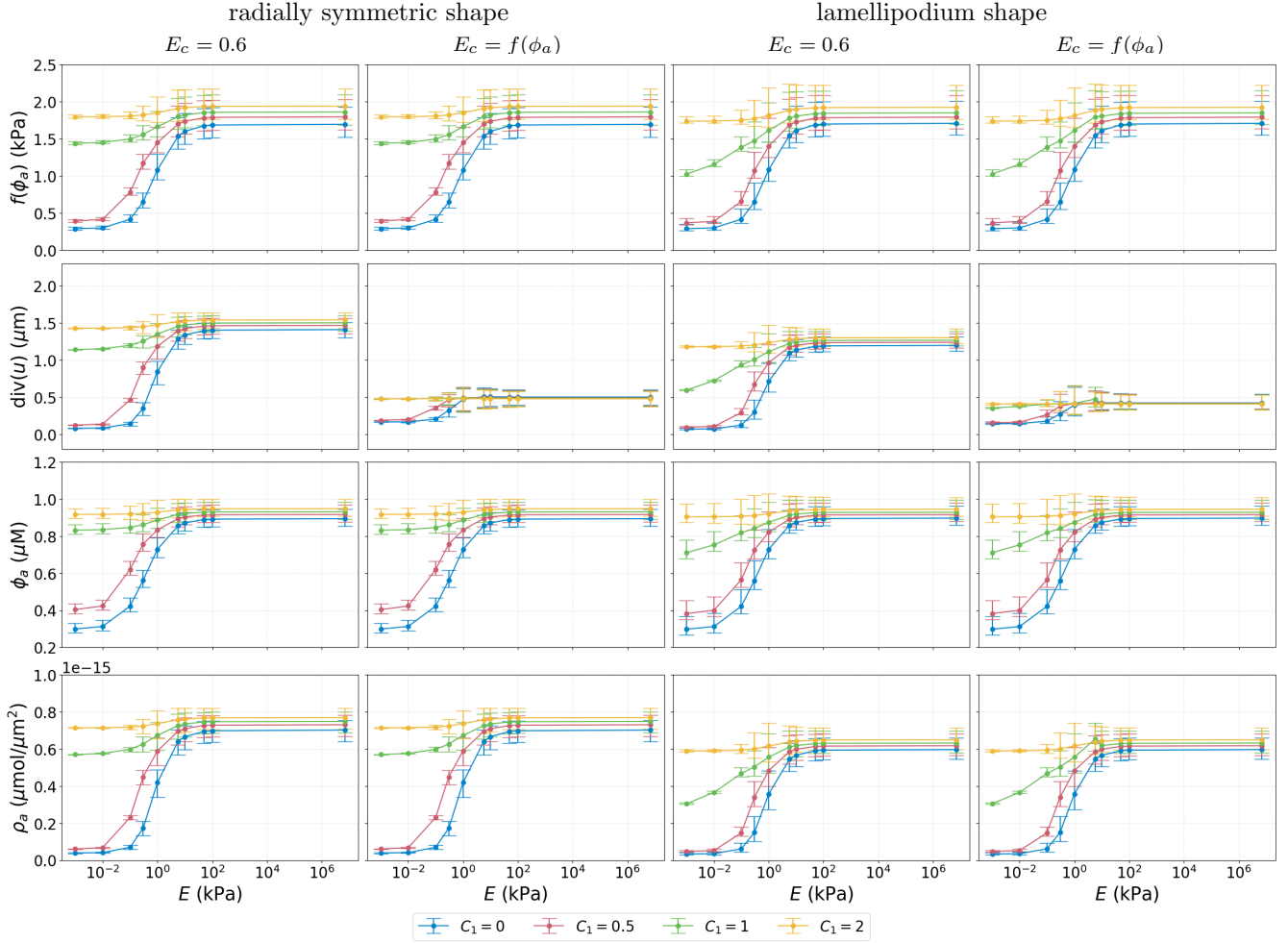


Figure 15: Simulation results of section 4.3.1 showing  $f(\phi_a)$ ,  $\text{div}(u)$ ,  $\phi_a$  and  $\rho_a$  as functions of substrate stiffness  $E$ , in the case of model (3), (4) and (6) and 3D stimulus, for different couplings, a range of values for  $C_1$ , and two different shapes at steady state for  $T = 100$  s. All other parameter values as in Tables 1 and 2.

### 4.3.2 Numerical simulations in the case of 2xD stimulus

In Figures 16–20 we report on simulation results in the case of 2xD stimulus and force boundary conditions applied to the entire boundary. For the concentrations, the results are similar to the results in the case of 2xD stimulus and no vertical deformation on the bottom of the cell, see Figures 1 and 16. However, the results for the deformation are different compared to the previous results. In Figure 16, the cell does not just expand but changes shape as the edges of the cell deform upwards, which is not possible in the case of the partially fixed boundary as we assume no vertical deformation at the base. The deformation of the cell upwards can also be observed in the case of the 3D stimulus, but it is smaller due to the impact of the ECM surrounding the cell, see Figure 11. We observe that for  $C_1 = 0$  the cell deforms upwards a little more than for  $C_1 = 1$ . This is due to the larger variation in the concentration  $\rho_a$  for  $C_1 = 0$  compared to  $C_1 = 1$ . The same features are observed for the lamellipodium shape, see Figure 3, 13, 18 and 20.

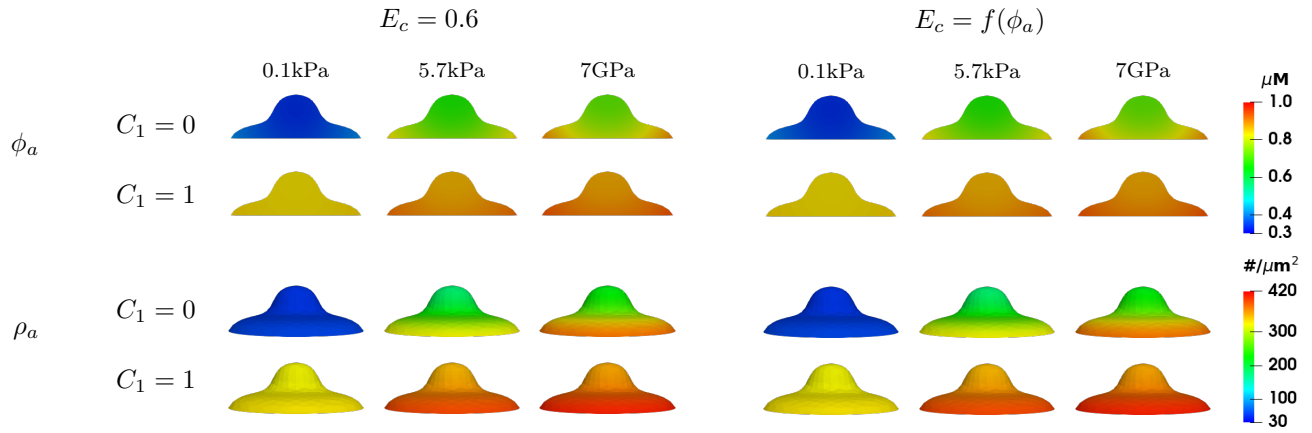


Figure 16: Numerical simulation results of section 4.3.2 showing  $\phi_a$  and  $\rho_a$  for model (3), (4), and (6) for the radially symmetric shape cells and 2xD stimulus at steady state for  $T = 100$  s. Four different scenario corresponding to  $C_1 = 0$  and  $C_1 = 1$ , and  $E_c = 0.6$  and  $E_c = f(\phi_a)$ . Within each figure, the rows are  $\phi_a$  and  $\rho_a$ , and the columns are  $E = 0.1, 5.7, 7 \cdot 10^6$  kPa. Parameter values as in Tables 1 and 2.

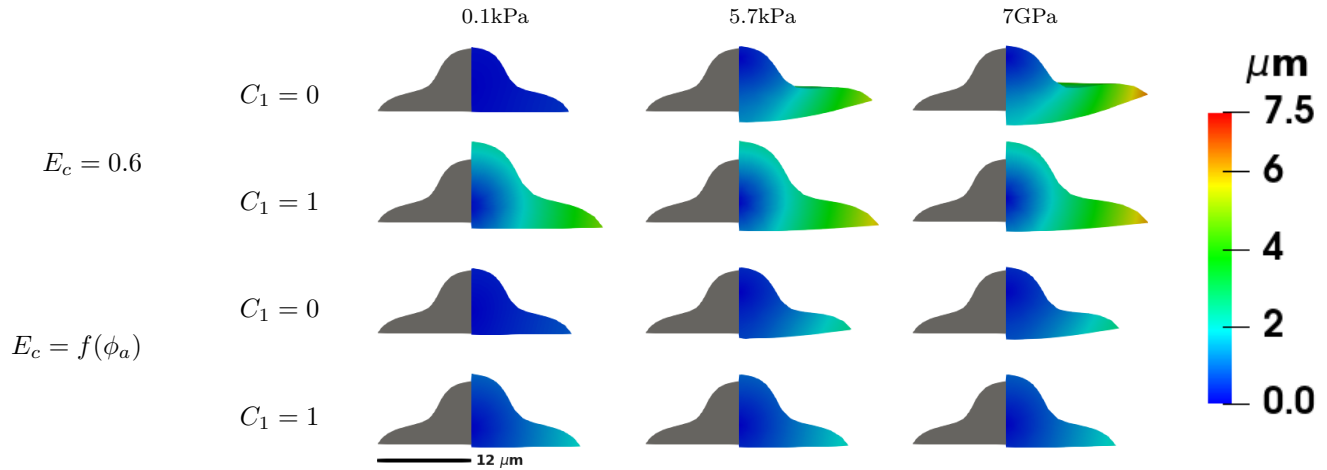


Figure 17: Numerical simulation results of section 4.3.2 showing  $u$  for model (3), (4), and (6) for the radially symmetric shape cells and 2xD stimulus at steady state for  $T = 100$  s. Four different scenario corresponding to  $C_1 = 0$  and  $C_1 = 1$ , and  $E_c = 0.6$  and  $E_c = f(\phi_a)$ . Within each figure the columns are  $E = 0.1, 5.7, 7 \cdot 10^6$  kPa. Parameter values as in Tables 1 and 2.

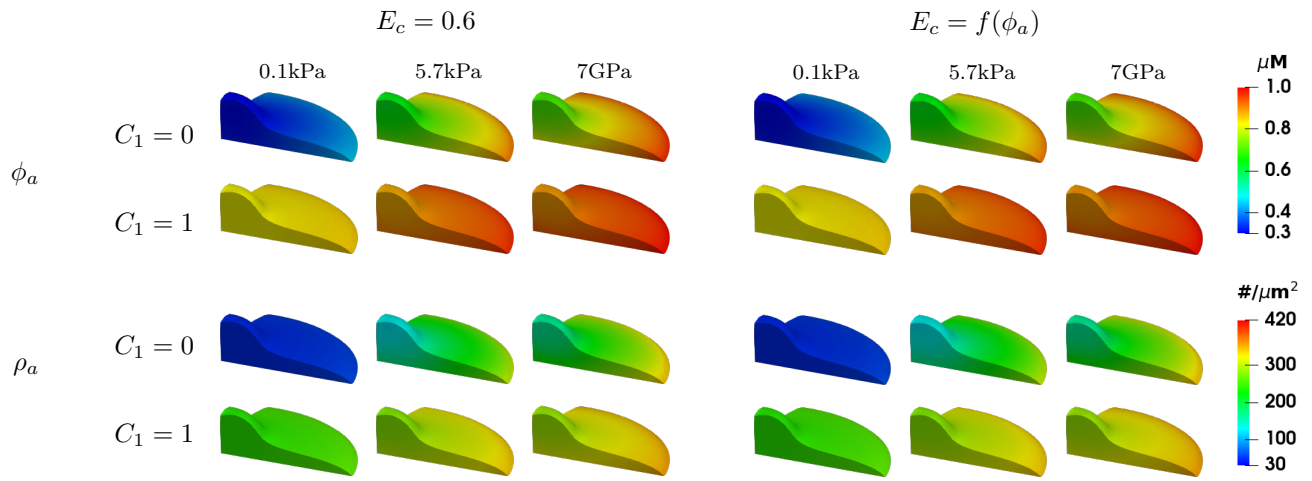


Figure 18: Numerical simulation results of section 4.3.2 showing  $\phi_a$  and  $\rho_a$  for model (3), (4), and (6) for the lamellipodium shape cells and 2xD stimulus at steady state for  $T = 100$  s. Four different scenario corresponding to  $C_1 = 0$  and  $C_1 = 1$ , and  $E_c = 0.6$  and  $E_c = f(\phi_a)$ . Within each figure, the rows are  $\phi_a$  and  $\rho_a$  and the columns are  $E = 0.1, 5.7, 7 \cdot 10^6$  kPa. Parameter values as in Tables 1 and 2.

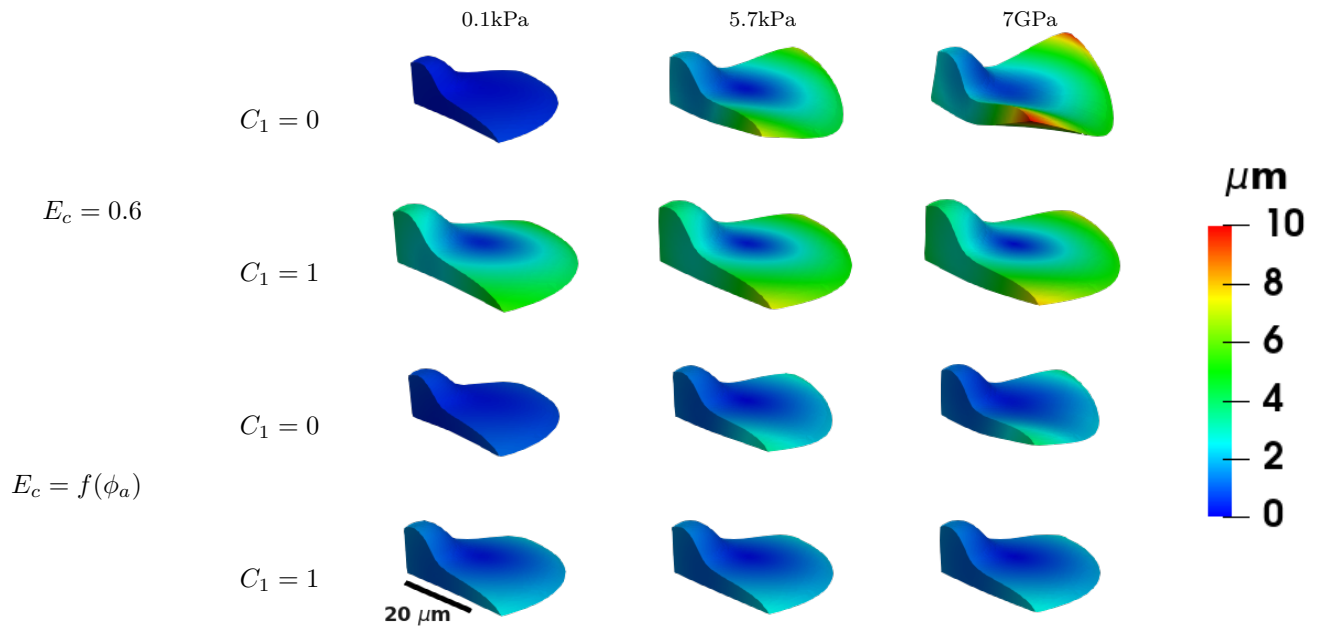


Figure 19: Numerical simulation results of section 4.3.2 showing  $u$  for model (3), (4), and (6) for the lamellipodium shape cells and 2xD stimulus at steady state for  $T = 100$  s. Four different scenario corresponding to  $C_1 = 0$  and  $C_1 = 1$ , and  $E_c = 0.6$  and  $E_c = f(\phi_a)$ . Within each figure the columns are  $E = 0.1, 5.7, 7 \cdot 10^6$  kPa. Parameter values as in Tables 1 and 2.



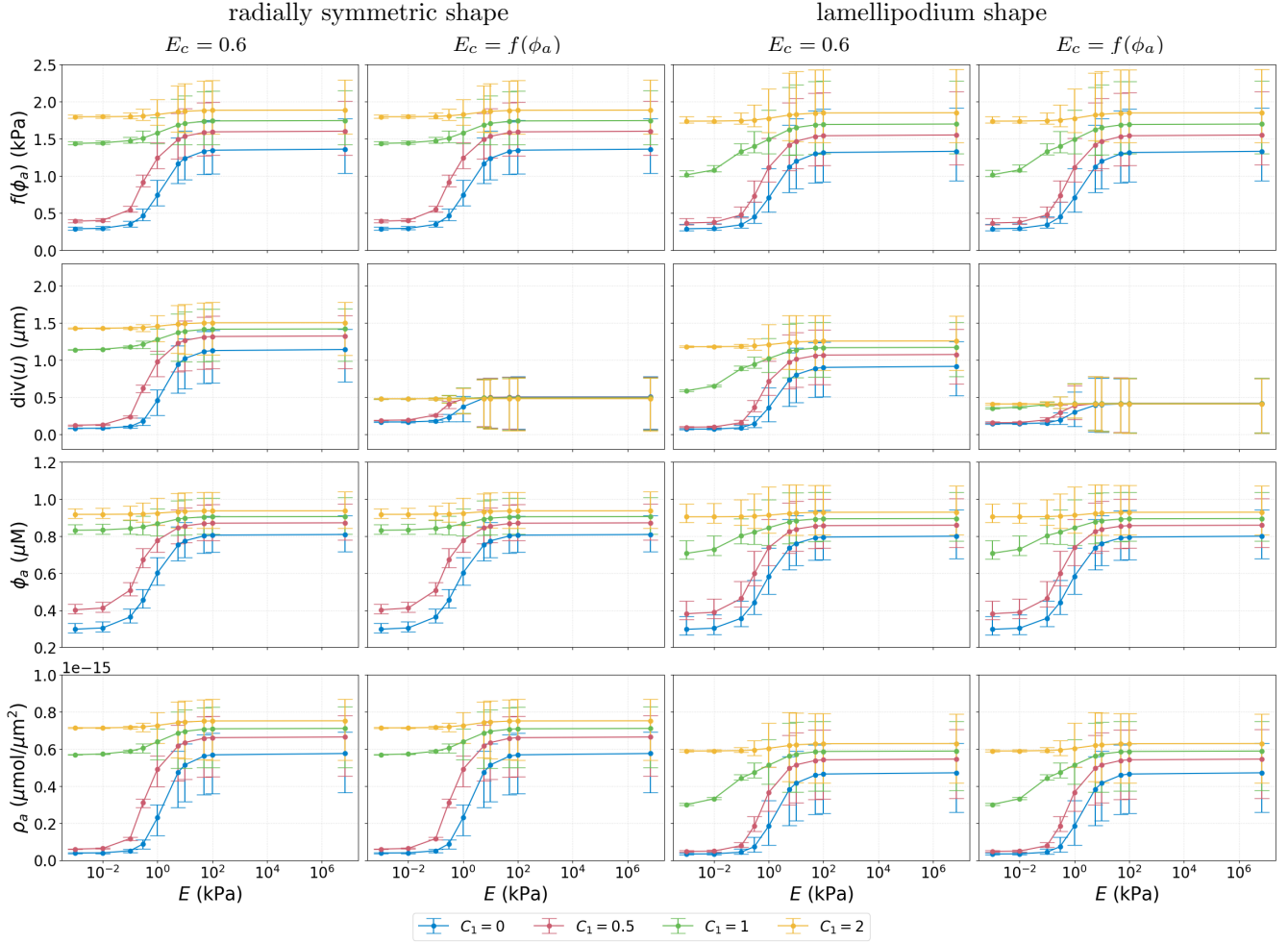


Figure 20: Simulation results of section 4.3.2 showing  $f(\phi_a)$ ,  $\text{div}(u)$ ,  $\phi_a$  and  $\rho_a$  as functions of substrate stiffness  $E$ , in the case of model (3), (4) and (6) and 2xD stimulus, for different couplings, a range of values for  $C_1$ , and two different shapes at steady state for  $T = 100$  s. All other parameter values as in Tables 1 and 2.

## 5 Discussion and Conclusion

We have derived a model for mechanotransduction via the RhoA signalling pathway with ECM stiffness and intracellular mechanical properties serving as the mechanical cues. The modelling extends the work of [SFR21] incorporating the explicit modelling of cell deformation based on an elastic constitutive assumption. We have extended on [SFR21; SSZ16; Ero+21] and introduced a two-way coupling between the mechanics of the cell and biochemical signalling processes. This two-way coupling appears to be central to mechanical homeostasis which is observed in biological experiments [Gro+23]. We propose a robust numerical method, based on the bulk-surface finite element method (FEM), see e.g. [DE13], for the approximation of the model and report on simulation results for different scenarios, validating the results by comparison with simulations presented in [SFR21] and experimental observations in [BCP17]. Namely, we considered different levels of substrate stiffness for cells of different shapes that either sit on a rigid flat substrate or are embedded in a three-dimensional substrate.

Our broad conclusions are that cell shape strongly influences the dynamics of the signalling molecules and the deformation of the cell, as seen in all figures comparing the radially symmetric and lamellipodium shape, where the emergent patterns differ, which is in line with experimental observations [Che+03; McB+04]. Cell shape also affects experimentally observed features such as the threshold-like response to changes in substrate stiffness [BCP17] which is reproduced by the model. In Figures 5, 10, 15 and 20, we see that for certain parameters ( $C_1 = 1$  and low substrate stiffness), the cell shape affects the mean concentrations of the signalling molecules and the mean deformation of the cell, and thus changes the threshold-like response.

Our simulations exhibit novel emergent features, that are inaccessible without the framework we propose, such

as the bidirectional coupling between mechanics and signalling processes through allowing the Young’s modulus of the cell to depend on protein concentration that can allow for robustness in terms of the magnitude of deformation in response to differences in substrate stiffness. This is an example of a mechanical homeostasis mechanism that emerges only at this level of modelling complexity which is of relevance to biology [Gro+23]. Other instances of mechanical homeostasis are the stress being maintained in the cardiovascular system under mechanical perturbations [Kas24] and the tensional homeostasis by the RhoA signalling pathway at the level of multiple cells [And+23; WG16], which is known to be governed by cellular stiffness sensing [Cha+24]. Another mechanism that experiences homeostatic response to substrate stiffness is that of the mechanical memory of the cell, describing the phenomenon of a cell responding less to substrates with lower stiffness if they have been cultured on stiff substrates [WG16; CGA22]. Due to the bidirectional coupling between the mechanics and the chemistry in our modelling framework, an extension of this work by changing the chosen couplings could be used to model these other mechanical homeostasis phenomena.

Based on previous biological studies [SFR21; Gar+04], we considered cases in which the mechanical properties of the cell (cell stiffness) depend on the local concentration of signalling molecules. This coupling yields less sensitivity of total deformation to substrate stiffness whilst leaving the dynamics of the signalling molecules themselves broadly unchanged, see Figures 5, 10, 15 and 20. The insensitivity of the dynamics of the signalling molecules to deformation levels arises since they are influenced by the local stress rather than deformation under our modelling. We note that the above constitutes another emergent homeostasis mechanism that the modelling framework allows us to explore. We stress that our work serves as an example of how mechanotransduction may be modelled and more complicated models for the mechanics, biochemistry and couplings therefore are warranted based on the remarkable emergent features we observe even in our relatively simple setting. We expect such models to be particularly fruitful avenues for future work.

The boundary conditions for the deformation we consider correspond to simple models of a cell in vitro (flat 2D substrate) or in vivo (homogeneous 3D matrix). We see that the cell on a 2D substrate appears to spread radially with minimal deformation orthogonal to the substrate while the latter exhibits a more uniform although smaller in total magnitude 3D deformation. Differences in deformation for different environments are in line with the literature as the effect of the substrate stiffness on cells is known to vary in 2D and 3D substrates [Byf+09]. An interesting extension that could be included in the above framework would be spatial variations in substrate stiffness or more complicated models for the substrate mechanics both of which are of much biological relevance [Cha+15; Ros+12].

This work shows how mechanistic modelling of mechanotransduction can reveal remarkable emergent properties. It lays the groundwork for future studies where further complexity can be added as required to model specific signalling pathways or to reflect other mechanical models derived from different constitutive assumptions. We anticipate that choosing a viscoelastic or poroelastic constitutive law for the mechanics of the cell is an interesting direction for future studies, as this is in line with recent experimental observations [Kas+07; Moe+13]. Given the fact that cell shape greatly influences the dynamics of the cell, as shown in this work, other reference geometries are also of interest as a subject for future work. Extending the signalling model of [SFR21] further, we intend to couple the model of this work with a similar biomechanical model for the deformation of the nucleus coupled with the dynamics of signalling molecules within the nucleus, such as the YAP/TAZ pathway [Jaf+24].

## Acknowledgments

SV was supported by the EPSRC Centre for Doctoral Training in Mathematical Modelling, Analysis and Computation (MAC-MIGS) funded by the UK Engineering and Physical Sciences Research Council (grant EP/S023291/1), Heriot-Watt University and the University of Edinburgh. CV acknowledges support from the Dr Perry James (Jim) Browne Research Centre on Mathematics and its Applications (University of Sussex).

SV and MP would like to thank the Isaac Newton Institute for Mathematical Sciences, Cambridge, for support and hospitality during the research programme ‘Uncertainty quantification and stochastic modelling of materials’, EPSRC Grant Number EP/R014604/1, where some work on the manuscript was undertaken.

The authors would like to thank Padmini Rangamani for helpful discussions.

## References

- [And+23] T. Andersen, D. Wörthmüller, D. Probst, I. Wang, P. Moreau, V. Fitzpatrick, T. Boudou, U. S. Schwarz, and M. Balland. “Cell size and actin architecture determine force generation in optogenetically activated cells”. In: *Biophysical Journal* 122.4 (2023), pp. 684–696. DOI: [10.1016/j.bpj.2023.01.011](https://doi.org/10.1016/j.bpj.2023.01.011).

- [AS14] P. J. Albert and U. S. Schwarz. “Dynamics of cell shape and forces on micropatterned substrates predicted by a cellular Potts model”. In: *Biophysical Journal* 106.11 (2014), pp. 2340–2352. DOI: [10.1016/j.bpj.2014.04.036](https://doi.org/10.1016/j.bpj.2014.04.036).
- [Bar+99] R. Bar-Ziv, T. Tlusty, E. Moses, S. A. Safran, and A. Bershadsky. “Pearling in cells: A clue to understanding cell shape”. In: *Proceedings of the National Academy of Sciences* 96.18 (1999), pp. 10140–10145. DOI: [10.1073/pnas.96.18.10140](https://doi.org/10.1073/pnas.96.18.10140).
- [BCP17] J. A. Beamish, E. Chen, and A. J. Putnam. “Engineered extracellular matrices with controlled mechanics modulate renal proximal tubular cell epithelialization”. In: *PLOS ONE* 12.7 (2017), e0181085. DOI: [10.1371/journal.pone.0181085](https://doi.org/10.1371/journal.pone.0181085).
- [BG16] K. Burrridge and C. Guilly. “Focal adhesions, stress fibers and mechanical tension”. In: *Experimental Cell Research* 343 (2016), pp. 14–20. DOI: [10.1016/j.yexcr.2015.10.029](https://doi.org/10.1016/j.yexcr.2015.10.029).
- [BM13] S. Banerjee and M. C. Marchetti. “Controlling cell–matrix traction forces by extracellular geometry”. In: *New Journal of Physics* 15.3 (2013), p. 035015. DOI: [10.1088/1367-2630/15/3/035015](https://doi.org/10.1088/1367-2630/15/3/035015).
- [BMG19] K. Burrridge, E. Monaghan-Benson, and D. M. Graham. “Mechanotransduction: from the cell surface to the nucleus via RhoA”. In: *Philosophical Transactions of the Royal Society B: Biological Sciences* 374.1779 (2019), p. 20180229. DOI: [10.1098/rstb.2018.0229](https://doi.org/10.1098/rstb.2018.0229).
- [BS07] A. Besser and U. S. Schwarz. “Coupling biochemistry and mechanics in cell adhesion: a model for inhomogeneous stress fiber contraction”. In: *New Journal of Physics* 9.11 (2007), pp. 425–425. DOI: [10.1088/1367-2630/9/11/425](https://doi.org/10.1088/1367-2630/9/11/425).
- [Byf+09] F. J. Byfield, R. K. Reen, T.-P. Shentu, I. Levitan, and K. J. Gooch. “Endothelial actin and cell stiffness is modulated by substrate stiffness in 2D and 3D”. In: *Journal of Biomechanics* 42.8 (2009), pp. 1114–1119. DOI: [10.1016/j.jbiomech.2009.02.012](https://doi.org/10.1016/j.jbiomech.2009.02.012).
- [CB96] M. Chrzanowska-Wodnicka and K. Burrridge. “Rho-stimulated contractility drives the formation of stress fibers and focal adhesions.” In: *Journal of Cell Biology* 133.6 (1996), pp. 1403–1415. DOI: [10.1083/jcb.133.6.1403](https://doi.org/10.1083/jcb.133.6.1403).
- [CGA22] L. Cacopardo, N. Guazzelli, and A. Ahluwalia. “Characterizing and Engineering Biomimetic Materials for Viscoelastic Mechanotransduction Studies”. In: *Tissue Engineering. Part B, Reviews* 28.4 (2022), pp. 912–925. DOI: [10.1089/ten.TEB.2021.0151](https://doi.org/10.1089/ten.TEB.2021.0151).
- [Cha+15] O. Chaudhuri, L. Gu, M. Darnell, D. Klumpers, S. A. Bencherif, J. C. Weaver, N. Huebsch, and D. J. Mooney. “Substrate stress relaxation regulates cell spreading”. In: *Nature Communications* 6.1 (2015), p. 6365. DOI: [10.1038/ncomms7365](https://doi.org/10.1038/ncomms7365).
- [Cha+24] M. Chanduri, A. Kumar, D. Weiss, N. Emuna, I. Barsukov, M. Shi, K. Tanaka, X. Wang, A. Datye, J. Kanyo, F. Collin, T. Lam, U. D. Schwarz, S. Bai, T. Nottoli, B. T. Goult, J. D. Humphrey, and M. A. Schwartz. “Cellular stiffness sensing through talin 1 in tissue mechanical homeostasis”. In: *Science Advances* 10.34 (2024), eadi6286. DOI: [10.1126/sciadv.adi6286](https://doi.org/10.1126/sciadv.adi6286).
- [Che+03] C. S. Chen, J. L. Alonso, E. Ostuni, G. M. Whitesides, and D. E. Ingber. “Cell shape provides global control of focal adhesion assembly”. In: *Biochemical and Biophysical Research Communications* 307.2 (2003), pp. 355–361. DOI: [10.1016/S0006-291X\(03\)01165-3](https://doi.org/10.1016/S0006-291X(03)01165-3).
- [Che+17] B. Cheng, M. Lin, G. Huang, Y. Li, B. Ji, G. M. Genin, V. S. Deshpande, T. J. Lu, and F. Xu. “Cellular mechanosensing of the biophysical microenvironment: A review of mathematical models of biophysical regulation of cell responses”. In: *Physics of Life Reviews* 22-23 (2017), pp. 88–119. DOI: [10.1016/j.plrev.2017.06.016](https://doi.org/10.1016/j.plrev.2017.06.016).
- [CSZ20] R. Chojowski, U. S. Schwarz, and F. Ziebert. “Reversible elastic phase field approach and application to cell monolayers”. In: *The European Physical Journal E* 43.10 (2020), p. 63. DOI: [10.1140/epje/i2020-11988-1](https://doi.org/10.1140/epje/i2020-11988-1).
- [CWM21] X. Cai, K.-C. Wang, and Z. Meng. “Mechanoregulation of YAP and TAZ in Cellular Homeostasis and Disease Progression”. In: *Front. Cell Dev. Biol.* 9 (2021), p. 673599. DOI: [10.3389/fcell.2021.673599](https://doi.org/10.3389/fcell.2021.673599).
- [DE13] G. Dziuk and C. M. Elliott. “Finite element methods for surface PDEs”. In: *Acta Numerica* 22 (2013), pp. 289–396. DOI: [10.1017/S0962492913000056](https://doi.org/10.1017/S0962492913000056).
- [Di+23] X. Di, X. Gao, L. Peng, J. Ai, X. Jin, S. Qi, H. Li, K. Wang, and D. Luo. “Cellular mechanotransduction in health and diseases: from molecular mechanism to therapeutic targets”. In: *Sig Transduct Target Ther* 8 (2023), p. 282. DOI: [10.1038/s41392-023-01501-9](https://doi.org/10.1038/s41392-023-01501-9).

- [Doy+15] A. D. Doyle, N. Carvajal, A. Jin, K. Matsumoto, and K. M. Yamada. “Local 3D matrix microenvironment regulates cell migration through spatiotemporal dynamics of contractility-dependent adhesions”. In: *J Cell Sci* 6 (2015), p. 8720. DOI: [10.1038/ncomms9720](https://doi.org/10.1038/ncomms9720).
- [Ero+21] K. S. Eroumé, R. Cavill, K. Staňková, J. de Boer, and A. Carlier. “Exploring the influence of cytosolic and membrane FAK activation on YAP/TAZ nuclear translocation”. In: *Biophysical Journal* 120.20 (2021), pp. 4360–4377. DOI: [10.1016/j.bpj.2021.09.009](https://doi.org/10.1016/j.bpj.2021.09.009).
- [Gar+04] M. L. Gardel, J. H. Shin, F. C. MacKintosh, L. Mahadevan, P. Matsudaira, and D. A. Weitz. “Elastic Behavior of Cross-Linked and Bundled Actin Networks”. In: *Science* 304.5675 (2004), pp. 1301–1305. DOI: [10.1126/science.1095087](https://doi.org/10.1126/science.1095087).
- [GB16] D. Graham and K. Burridge. “Mechanotransduction and nuclear function”. In: *Current Opinion in Cell Biology* 40 (2016), pp. 98–105. DOI: [10.1016/j.ceb.2016.03.006](https://doi.org/10.1016/j.ceb.2016.03.006).
- [Gil+06] D. Gilbert, H. Fuss, X. Gu, R. Orton, S. Robinson, V. Vyshemirsky, M. J. Kurth, C. S. Downes, and W. Dubitzky. “Computational methodologies for modelling, analysis and simulation of signalling networks”. In: *Briefings in Bioinformatics* 7.4 (2006), pp. 339–353. DOI: [10.1093/bib/bbl043](https://doi.org/10.1093/bib/bbl043).
- [GJG14] P. García-Penarrubia, J. J. J. Gálvez, and J. Gálvez. “Mathematical modelling and computational study of two-dimensional and three-dimensional dynamics of receptor–ligand interactions in signalling response mechanisms”. In: *J. Math. Biol.* 69 (2014), pp. 553–582.
- [Gou13] P. L. Gould. *Introduction to Linear Elasticity*. New York, NY: Springer New York, 2013. DOI: [10.1007/978-1-4614-4833-4](https://doi.org/10.1007/978-1-4614-4833-4).
- [GR09] C. Geuzaine and J.-F. Remacle. “Gmsh: A 3-D finite element mesh generator with built-in pre- and post-processing facilities”. In: *International Journal for Numerical Methods in Engineering* 79.11 (2009), pp. 1309–1331. DOI: [10.1002/nme.2579](https://doi.org/10.1002/nme.2579).
- [Gro+23] J. Grolleman, N. van Engeland, M. Raza, S. Azimi, V. Conte, C. Sahlgren, and C. Bouten. “Environmental stiffness restores mechanical homeostasis in vimentin-depleted cells”. In: *Nature, Scientific Reports* 13 (2023), p. 18374. DOI: [10.1038/s41598-023-44835-8](https://doi.org/10.1038/s41598-023-44835-8).
- [GW17] P. Gilbert and V. Weaver. “Cellular adaptation to biomechanical stress across length scales in tissue homeostasis and disease”. In: *Seminars Cell Develop. Biol.* 67 (2017), pp. 141–152. DOI: [10.1016/j.semcdb.2016.09.004](https://doi.org/10.1016/j.semcdb.2016.09.004).
- [HDS14] J. D. Humphrey, E. R. Dufresne, and M. A. Schwartz. “Mechanotransduction and extracellular matrix homeostasis”. In: *Nature reviews. Molecular cell biology* 15.12 (2014), pp. 802–812. DOI: [10.1038/nrm3896](https://doi.org/10.1038/nrm3896).
- [Jaf+24] H. Jafarinia, A. Khalilimeybodi, J. Barrasa-Fano, S. I. Fraley, P. Rangamani, and A. Carlier. “Insights gained from computational modeling of YAP/TAZ signaling for cellular mechanotransduction”. In: *npj Systems Biology and Applications* 10.1 (2024), pp. 1–14. DOI: [10.1038/s41540-024-00414-9](https://doi.org/10.1038/s41540-024-00414-9).
- [Kan+15] J. Kang, K. M. Puskar, A. J. Ehrlicher, P. R. LeDuc, and R. S. Schwartz. “Structurally Governed Cell Mechanotransduction through Multiscale Modeling”. In: *Scientific Reports* 5.1 (2015), p. 8622. DOI: [10.1038/srep08622](https://doi.org/10.1038/srep08622).
- [Kas+07] K. E. Kasza, A. C. Rowat, J. Liu, T. E. Angelini, C. P. Brangwynne, G. H. Koenderink, and D. A. Weitz. “The cell as a material”. In: *Current Opinion in Cell Biology* 19.1 (2007), pp. 101–107. DOI: [10.1016/j.ceb.2006.12.002](https://doi.org/10.1016/j.ceb.2006.12.002).
- [Kas24] G. S. Kassab. “Biomechanical Homeostasis”. In: *Coronary Circulation: Mechanobiology, Growth, Remodeling, and Clinical Implications*. Ed. by G. S. Kassab. Cham: Springer International Publishing, 2024, pp. 1–43. DOI: [10.1007/978-3-031-62652-4\\_1](https://doi.org/10.1007/978-3-031-62652-4_1).
- [Le +12] S. E. Le Dévédec, B. Geverts, H. de Bont, K. Yan, F. J. Verbeek, A. B. Houtsmuller, and B. van de Water. “The residence time of focal adhesion kinase (FAK) and paxillin at focal adhesions in renal epithelial cells is determined by adhesion size, strength and life cycle status”. In: *Journal of Cell Science* 125 (2012), pp. 4498–4506. DOI: [10.1242/jcs.104273](https://doi.org/10.1242/jcs.104273).
- [LMV13] O. Lakkis, A. Madzvamuse, and C. Venkataraman. “Implicit-explicit timestepping with finite element approximation of reaction-diffusion systems on evolving domains”. In: *SIAM Journal on Numerical Analysis* 51.4 (2013), pp. 2309–2330. DOI: [10.1137/120880112](https://doi.org/10.1137/120880112).

- [LMW12] A. Logg, K.-A. Mardal, and G. Wells, eds. *Automated Solution of Differential Equations by the Finite Element Method*. Vol. 84. Lecture Notes in Computational Science and Engineering. Berlin, Heidelberg: Springer Berlin Heidelberg, 2012. DOI: [10.1007/978-3-642-23099-8](https://doi.org/10.1007/978-3-642-23099-8).
- [Mar+18] F. Martino, A. R. Perestrelo, V. Vinarský, S. Pagliari, and G. Forte. “Cellular Mechanotransduction: From Tension to Function”. In: *Frontiers in Physiology* 9 (2018).
- [McB+04] R. McBeath, D. M. Pirone, C. M. Nelson, K. Bhadriraju, and C. S. Chen. “Cell Shape, Cytoskeletal Tension, and RhoA Regulate Stem Cell Lineage Commitment”. In: *Developmental Cell* 6.4 (2004), pp. 483–495. DOI: [10.1016/S1534-5807\(04\)00075-9](https://doi.org/10.1016/S1534-5807(04)00075-9).
- [MDS25] G. R. McNicol, M. J. Dalby, and P. S. Stewart. “A theoretical model for focal adhesion and cytoskeleton formation in non-motile cells”. In: *Journal of Theoretical Biology* 596 (2025), p. 111965. DOI: [10.1016/j.jtbi.2024.111965](https://doi.org/10.1016/j.jtbi.2024.111965).
- [Moe+13] E. Moeendarbary, L. Valon, M. Fritzsche, A. R. Harris, D. A. Moulding, A. J. Thrasher, E. Stride, L. Mahadevan, and G. T. Charras. “The cytoplasm of living cells behaves as a poroelastic material”. In: *Nature Materials* 12.3 (2013), pp. 253–261. DOI: [10.1038/nmat3517](https://doi.org/10.1038/nmat3517).
- [Nov+21] J. K. Novev, M. L. Heltberg, M. H. Jensen, and A. Doostmohammadi. “Spatiotemporal model of cellular mechanotransduction via Rho and YAP”. In: *Integrative Biology* 13.8 (2021), pp. 197–209. DOI: [10.1093/intbio/zyab012](https://doi.org/10.1093/intbio/zyab012).
- [Oak+14] P. W. Oakes, S. Banerjee, M. C. Marchetti, and M. L. Gardel. “Geometry Regulates Traction Stresses in Adherent Cells”. In: *Biophysical Journal* 107.4 (2014), pp. 825–833. DOI: [10.1016/j.bpj.2014.06.045](https://doi.org/10.1016/j.bpj.2014.06.045).
- [PV20] M. Ptashnyk and C. Venkataraman. “Multiscale Analysis and Simulation of a Signaling Process With Surface Diffusion”. In: *Multiscale Modeling & Simulation* 18.2 (2020), pp. 851–886. DOI: [10.1137/18M1185661](https://doi.org/10.1137/18M1185661).
- [Rom+21] P. Romani, L. Valcarcel-Jimenez, C. Frezza, and S. Dupont. “Crosstalk between mechanotransduction and metabolism”. In: *Nature Reviews Molecular Cell Biology* 22.1 (2021), pp. 22–38. DOI: [10.1038/s41580-020-00306-w](https://doi.org/10.1038/s41580-020-00306-w).
- [Ros+12] A. M. Ross, Z. Jiang, M. Bastmeyer, and J. Lahann. “Physical Aspects of Cell Culture Substrates: Topography, Roughness, and Elasticity”. In: *Small* 8.3 (2012), pp. 336–355. DOI: [10.1002/sml1.201100934](https://doi.org/10.1002/sml1.201100934).
- [SFR21] K. E. Scott, S. I. Fraley, and P. Rangamani. “A spatial model of YAP/TAZ signaling reveals how stiffness, dimensionality, and shape contribute to emergent outcomes”. In: *Proceedings of the National Academy of Sciences* 118.20 (2021), e2021571118. DOI: [10.1073/pnas.2021571118](https://doi.org/10.1073/pnas.2021571118).
- [SGF16] Z. Sun, S. Guo, and R. Fässler. “Integrin-mediated mechanotransduction”. In: *J Cell Biol.* 215.4 (2016), pp. 445–456. DOI: [10.1083/jcb.201609037](https://doi.org/10.1083/jcb.201609037).
- [SIC23] A. Saraswathibhatla, D. Indana, and O. Chaudhuri. “Cell–extracellular matrix mechanotransduction in 3D”. In: *Nature Reviews Molecular Cell Biology* 24.7 (2023), pp. 495–516. DOI: [10.1038/s41580-023-00583-1](https://doi.org/10.1038/s41580-023-00583-1).
- [SSZ16] M. Sun, F. Spill, and M. H. Zaman. “A Computational Model of YAP/TAZ Mechanosensing”. In: *Biophysical Journal* 110.11 (2016), p. 2540. DOI: [10.1016/j.bpj.2016.04.040](https://doi.org/10.1016/j.bpj.2016.04.040).
- [Tom+09] A. Tomar, S. Lim, Y. Lim, and D. Schlaepfer. “A FAK-p120RasGAP-p190RhoGAP complex regulates polarity in migrating cells”. In: *Journal of Cell Science* 122 (2009), pp. 1852–1862. DOI: [10.1242/jcs.046870](https://doi.org/10.1242/jcs.046870).
- [VE22] P. Valls and A. Esposito. “Signalling dynamics, cell decisions, and homeostatic control in health and disease”. In: *J Cell Sci Curr Opin Cell Biol* 75 (2022), p. 102066. DOI: [10.1016/j.ceb.2022.01.011](https://doi.org/10.1016/j.ceb.2022.01.011).
- [Via+10] B. Vianay, J. Käfer, E. Planus, M. Block, F. Graner, and H. Guillou. “Single Cells Spreading on a Protein Lattice Adopt an Energy Minimizing Shape”. In: *Physical Review Letters* 105.12 (2010), p. 128101. DOI: [10.1103/PhysRevLett.105.128101](https://doi.org/10.1103/PhysRevLett.105.128101).
- [WG16] V. M. Weaver and P. M. Gilbert. “Cellular adaptation to biomechanical stress across length scales in tissue homeostasis and disease”. In: *Seminars in cell & developmental biology* 67 (2016), p. 141. DOI: [10.1016/j.semcd.2016.09.004](https://doi.org/10.1016/j.semcd.2016.09.004).

- [Xie+23] N. Xie, C. Xiao, Q. Shu, B. Cheng, Z. Wang, R. Xue, Z. Wen, J. Wang, H. Shi, D. Fan, N. Liu, and F. Xu. “Cell response to mechanical microenvironment cues via Rho signaling: From mechanobiology to mechanomedicine”. In: *Acta Biomaterialia* 159 (2023), pp. 1–20. DOI: [10.1016/j.actbio.2023.01.039](https://doi.org/10.1016/j.actbio.2023.01.039).
- [YR23] K. Young and C. Reinhart-King. “Environmental stiffness restores mechanical homeostasis in vimentin-depleted cells”. In: *Current Opinion in Cell Biology* 83 (2023), p. 102208. DOI: [10.1016/j.ceb.2023.102208](https://doi.org/10.1016/j.ceb.2023.102208).
- [Zha+07] X.-H. Zhao, C. Laschinger, P. Arora, K. Szászi, A. Kapus, and C. A. McCulloch. “Force activates smooth muscle  $\alpha$ -actin promoter activity through the Rho signaling pathway”. In: *J Cell Sci* 120 (2007), pp. 1801–1809. DOI: [10.1242/jcs.001586](https://doi.org/10.1242/jcs.001586).

# A Appendix

## A.1 Comparison of the reduced model and the full model of [SFR21]

We verify the reduced model (1) captures the results obtained in [SFR21] for the full model for the RhoA signalling pathway. In numerical simulations of model (1) we use the same parameter values as in [SFR21], except for the diffusion coefficients  $D_1$  and  $D_2$  for activated and deactivated FAK. It is suggested in the literature that  $D_1 = D_2 = 4 \mu\text{m}^2/\text{s}$  [Le +12], but [SFR21] uses  $10 \mu\text{m}^2/\text{s}$  due to computational issues. Thus in our numerical simulations we consider both diffusion coefficients.

$\phi_d^0 = 0.7 \mu\text{M}$	$C = 3.25 \text{ kPa}$ $\gamma = 77.56 \mu\text{M}^{-5}$ $n = 5$ $E = 0.1, 5.7, 7 \cdot 10^6 \text{ kPa}$	$D_1 = 4 \text{ or } 10 \mu\text{m}^2/\text{s}$	$k_2 = 0.015 \frac{ Y }{ \Gamma } \text{ s}^{-1}$ $k_3 = 0.379 \frac{ Y }{ \Gamma } \text{ s}^{-1}$ $k_4 = 0.625 \text{ s}^{-1}$ $k_5 = 0.0168 \frac{ Y }{ \Gamma } \text{ s}^{-1}$
$\phi_a^0 = 0.3 \mu\text{M}$		$D_2 = 4 \text{ or } 10 \mu\text{m}^2/\text{s}$	
$\rho_a^0 = 33.6 \#/\mu\text{m}^2$		$D_3 = 0.3 \mu\text{m}^2/\text{s}$	
$\approx 0.06 \cdot 10^{-5} \frac{\mu\text{mol}}{\text{dm}^3}$		$k_1 = 0.035 \text{ s}^{-1}$	

Table A1: Parameter values for model (1).

The model (1) is implemented in FEniCS [LMW12], using a Finite Element Method for discretization in space and IMEX time-stepping method to discretize in time, see Appendix A.3 for more details. Considering domain  $Y \subset \mathbb{R}^3$ , denoting the cytoplasm, and  $\Gamma = \partial Y$ , defining the cell membrane, and times interval  $(0, T)$ , with  $T = 100\text{s}$ , for the space discretisation we choose meshsize  $h = 2.94$  and time step  $\Delta t = 0.5$  for the backwards Euler discretisation in time. For our domain we have  $n_r = |Y|/|\Gamma| = 1.17$ . We consider three different stimuli, similar to [SFR21], (i) the ‘2D stimulus’, where the substrate stiffness is only applied to the bottom of the cell and any reaction terms of RhoA are nonzero only at the bottom of the cell, (ii) the ‘2xD stimulus’, where the substrate stiffness is only applied to the bottom of the cell but the reaction terms of RhoA on the whole cell membrane, and (iii) the ‘3D stimulus’ where the cell is embedded in an agar (substrate) and the impact of the substrate stiffness on the signalling processes is considered on the whole cell membrane.

Comparing the simulation results for reduced model (1) in Figures A1 and A2 to the results presented in [SFR21, Figure 3] for the full model, the dynamics of FAK and RhoA are almost identical qualitatively. Similar to the results in [SFR21, Figure 3], the highest concentration of both  $\phi_a$  and  $\rho_a$  is at the edges of the cell. Also, there is threshold value of  $E \approx 1\text{kPa}$ , below which the concentrations of  $\phi_a$  and  $\rho_a$  stay close to the initial values and then reaches high steady states values, similar for both  $E = 5.7\text{kPa}$  and  $E = 7\text{GPa}$ . Quantitatively, the values for  $\phi_a$  are also close to the one reported in [SFR21, Figure 3]. This suggests that the reduction of the model as well as considering the whole cell domain without excluding a nucleus does not have significant effect on the dynamics of FAK. However, for  $\rho_a$  we obtain slightly lower concentration, where the maximum concentration in our results is  $420 \#/\mu\text{m}^2$  and the maximum concentration in [SFR21, Fig.3] is  $593 \#/\mu\text{m}^2$ . This difference could be related to the model reduction and approximation for the deactivated RhoA. However, the method to convert from  $\mu\text{mol}/L$  to  $\#/\mu\text{m}^2$  is not clearly explained in [SFR21] and may also contribute to the difference in the maximal values, see Appendix A.4 for the details on the conversion  $\mu\text{mol}/L$  to  $\#/\mu\text{m}^2$  used in model (1).

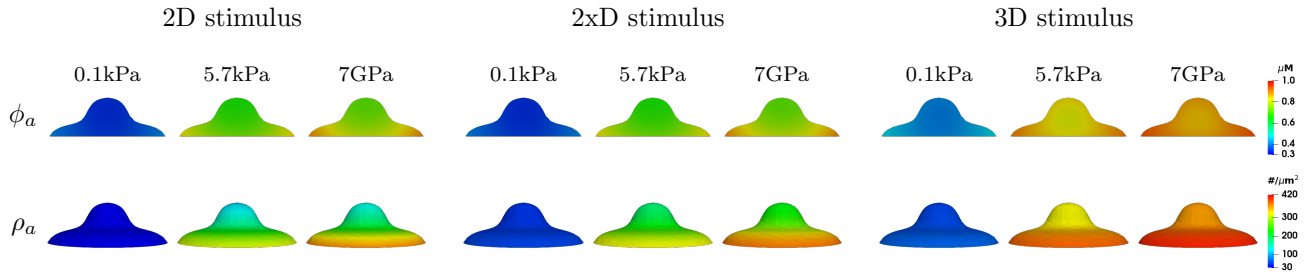


Figure A1: Numerical simulation results of Appendix A.1 showing  $\phi_a$  and  $\rho_a$  for reduced model (1) at steady state for  $T = 100 \text{ s}$ . Parameter values as in Table A1 and  $D_1 = D_2 = 4 \mu\text{m}^2/\text{s}$ .

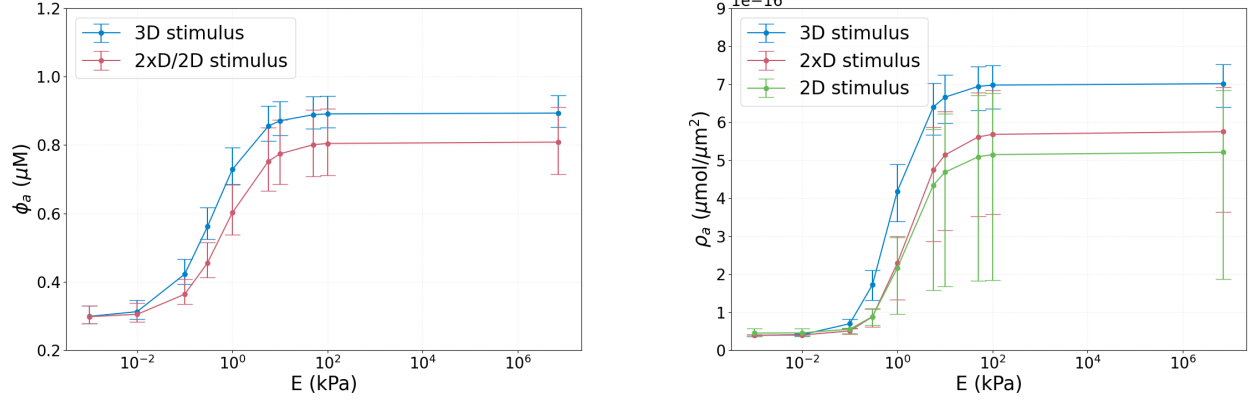


Figure A2: Results of Appendix A.1 showing the effect of substrate stiffness  $E$  on  $\phi_a$  and  $\rho_a$  for the reduced model (1) at steady state for  $T = 100$  s. Parameter values as in Table A1 with  $D_1 = D_2 = 4 \mu\text{m}^2/\text{s}$ .

Simulation results for the reduced model with diffusion coefficients  $D_1 = D_2 = 10 \mu\text{m}^2/\text{s}$  are presented in Figures A3 and A4. Comparing Figures A2 and A4, we see that the averaged over space dynamics are very similar, but numerical simulation results for a lower diffusion coefficient show lower minimum and higher maximum concentrations, which can be explain by the fact that slower diffusion of  $\phi_a$  causes stronger heterogeneity across the cell domain. In Figures A1 and A3, we observe the same dynamics for both diffusion coefficients, where the maximum concentration is at the edges of the cell and the minimum concentration is in the middle. Since the dynamics of  $\rho_a$  depends on  $\phi_a$ , similar results are obtain for  $\rho_a$ .

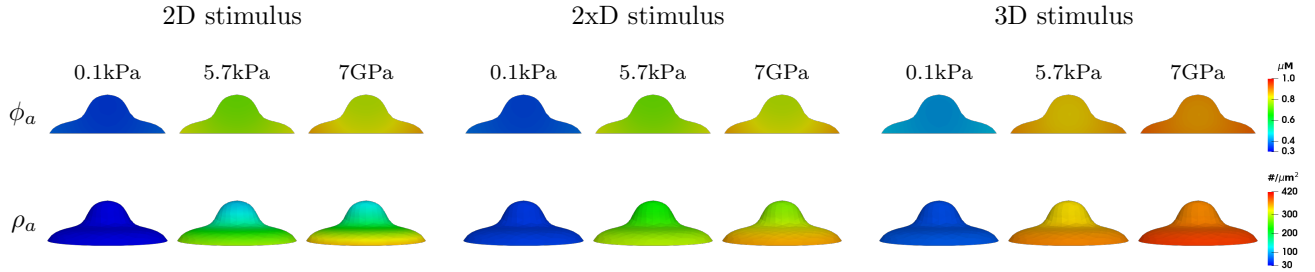


Figure A3: Numerical simulation results of Appendix A.1 showing  $\phi_a$  and  $\rho_a$  for reduced model (1) at steady state for  $T = 100$  s. Parameter values as in Table A1 with  $D_1 = D_2 = 10 \mu\text{m}^2/\text{s}$ .

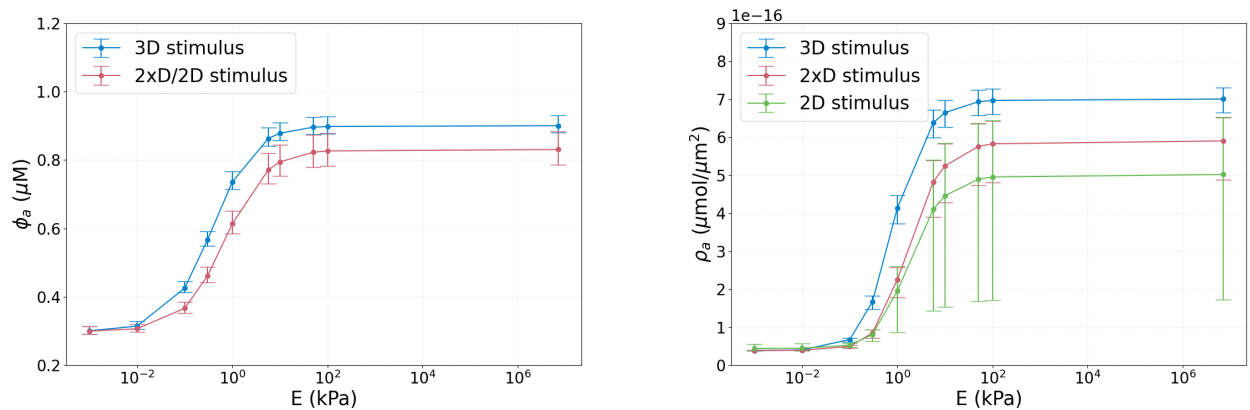


Figure A4: Results of Appendix A.1 showing effect of substrate stiffness  $E$  on  $\phi_a$  and  $\rho_a$  for the reduced model (1) at steady state for  $T = 100$  s. Parameter values as in Table A1 with  $D_1 = D_2 = 10 \mu\text{m}^2/\text{s}$ .



## A.2 Temporal statistics

Figure A5 shows the evolution of the mean of  $f(\phi_a)$ ,  $\text{div}(u)$ ,  $\phi_a$  and  $\rho_a$  over time for different couplings and parameters for the radially symmetric cell shape.

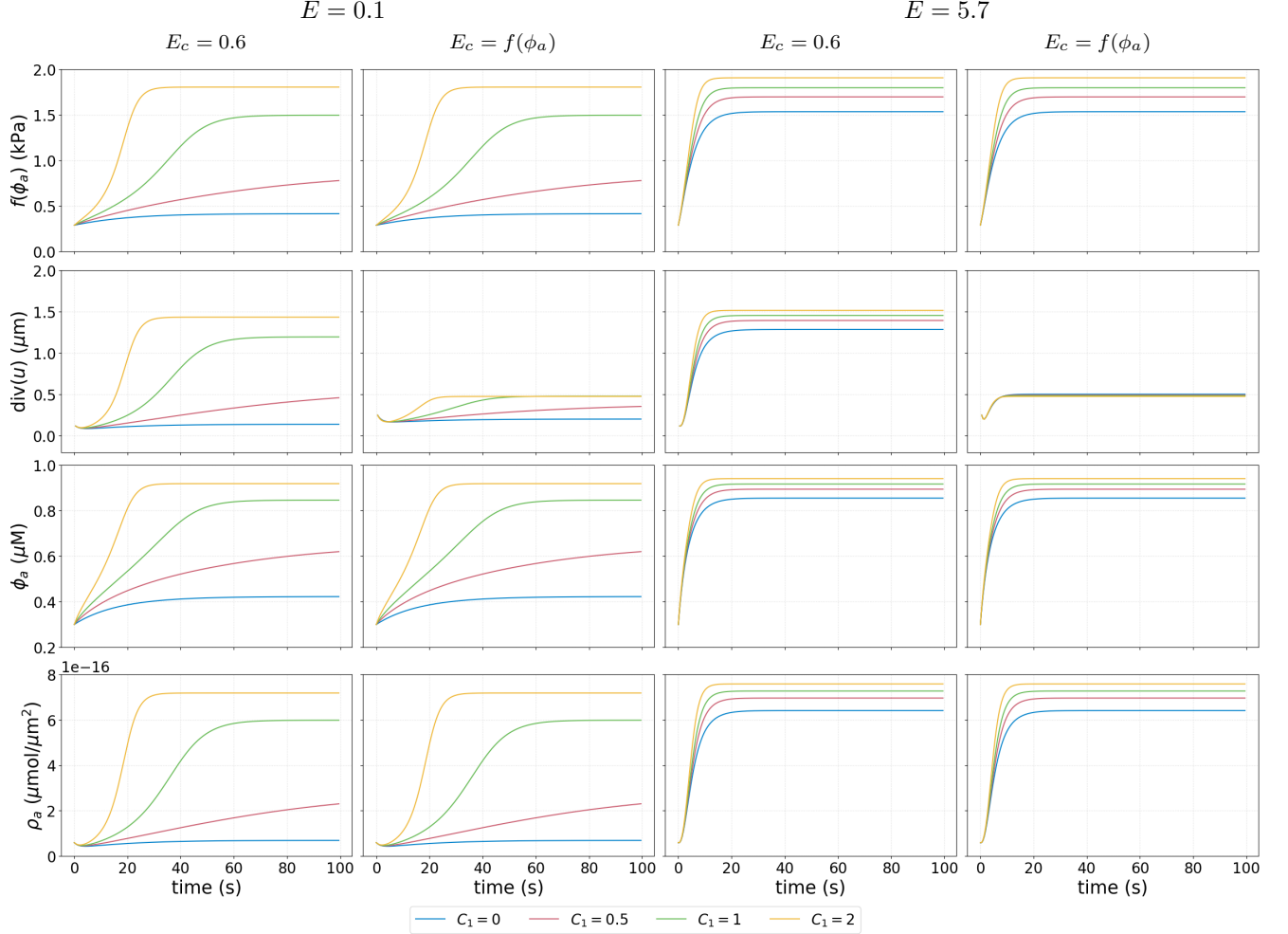


Figure A5: Simulations results of Appendix A.2 showing the mean of  $f(\phi_a)$ ,  $\text{div}(u)$ ,  $\phi_a$  and  $\rho_a$  as functions of time, in the case of model (3), (4) and (6), radially symmetric shape and 3D stimulus, for different couplings, a range of values for  $C_1$ , and two different values for the substrate stiffness  $E$ . All other parameter values as in Tables 1 and 2. The corresponding results can be found in Figures 11 and 12.

## A.3 Numerical Scheme

For numerical simulations of model (3)-(6) we use FEM for discretization in space and backward Euler for discretization in time, implemented in FEniCS [LMW12]. Consider the space

$$\mathcal{W}(Y) = \{u \in H^1(Y) : \int_Y u \, d\xi = 0, \int_Y (\partial_{x_j} u_i - \partial_{x_i} u_j) \, d\xi = 0 \text{ for } i, j = 1, 2, 3\}, \quad (7)$$

such that  $\mathcal{W}(Y) \cap \mathcal{R}(Y) = 0$  with  $\mathcal{R}(Y)$  the space of rigid motions. Then, the weak formulation of the model (3)-(6) is given for  $(\phi_d, \phi_a) \in L^2(0, T; H^1(Y))$ ,  $\rho_a \in L^2(0, T; H^1(\Gamma))$ , with  $(\partial_t \phi_d, \partial_t \phi_a) \in L^2(0, T; H^1(Y)')$  and  $\partial_t \rho_a \in L^2(0, T; H^1(\Gamma)')$ , and  $u \in L^2(0, T; \mathcal{W}(Y))$  satisfying

$$\begin{aligned} \langle \partial_t \phi_d, \psi \rangle_{(H^1)', T} + \langle D_1 \nabla \phi_d, \nabla \psi \rangle_{Y_T} + \langle C_1 \text{tr}(\sigma(u))_+ \phi_d, \psi \rangle_{Y_T} + \langle k_3 \phi_d, \psi \rangle_{\Gamma_T} &= \langle k_1 \phi_a, \psi \rangle_{Y_T}, \\ \langle \partial_t \phi_a, \psi \rangle_{(H^1)', T} + \langle D_2 \nabla \phi_a, \nabla \psi \rangle_{Y_T} + \langle k_1 \phi_a, \psi \rangle_{Y_T} &= \langle C_1 \text{tr}(\sigma(u))_+ \phi_d, \psi \rangle_{Y_T} + \langle k_3 \phi_d, \psi \rangle_{\Gamma_T}, \\ \langle \partial_t \rho_a, w \rangle_{(H^1)', T} + \langle D_3 \nabla_{\Gamma} \rho_a, \nabla_{\Gamma} w \rangle_{\Gamma_T} + \langle k_4(\phi_a) \rho_a, w \rangle_{\Gamma_T} &= \langle k_5(\phi_a), w \rangle_{\Gamma_T}, \\ \langle E(\phi_a) \epsilon(u), \epsilon(v) \rangle_{Y_T} &= \langle \mathbb{P}(k_6 \rho_a \nu), v \rangle_{\Gamma_T}, \end{aligned} \quad (8)$$

for all  $\psi \in L^2(0, T; H^1(Y))$ ,  $w \in L^2(0, T; H^1(\Gamma))$ , and  $v \in L^2(0, T; H^1(Y))$ , with initial conditions satisfied in the  $L^2$ -sense. Here  $\langle \phi, \psi \rangle_{(H^1)', T}$  denotes the dual product between  $\phi \in L^2(0, T; H^1(Y))$  and  $\psi \in L^2(0, T; H^1(Y)')$  or between  $\phi \in L^2(0, T; H^1(\Gamma))$  and  $\psi \in L^2(0, T; H^1(\Gamma)')$  and

$$\langle \phi, \psi \rangle_{Y_T} = \int_0^T \int_Y \phi \psi dx dt, \quad \langle \psi_1, \psi_1 \rangle_{\Gamma_T} = \int_0^T \int_{\Gamma} v w dx dt, \quad \text{where } 1/p_1 + 1/p_2 = 1, \quad 1/q_1 + 1/q_2 = 1,$$

for  $\phi \in L^{p_1}(0, T; L^{q_1}(Y))$ ,  $\psi \in L^{p_2}(0, T; L^{q_2}(Y))$ ,  $\phi_1 \in L^{p_1}(0, T; L^{q_1}(\Gamma))$ , and  $\psi_1 \in L^{p_2}(0, T; L^{q_2}(\Gamma))$ . The discretization of the domain is given by the polyhedral approximation of  $Y$  such that  $Y_h$  is the union of finitely many tetrahedrons in  $\mathbb{R}^3$ , and  $S_h$  is the set of these tetrahedrons  $K$ , such that

$$Y_h = \bigcup_{K \in S_h} K.$$

Then the surface  $\Gamma$  is approximated by  $\Gamma_h$  such that  $\Gamma_h = \partial Y_h$ . The mesh size is defined by the maximum diameter of a simplex  $h = \max\{h_Y, h_{\Gamma}\}$ , where  $h_Y = \max_{K \in S_h} h_Y(K)$  and  $h_{\Gamma} = \max_{R=K \cap \Gamma_h \neq \emptyset, K \in S_h} h_{\Gamma}(R)$  with  $h_Y(K)$  being the diameter of a tetrahedron and  $h_{\Gamma}(R)$  the diameter of a triangle on the surface.

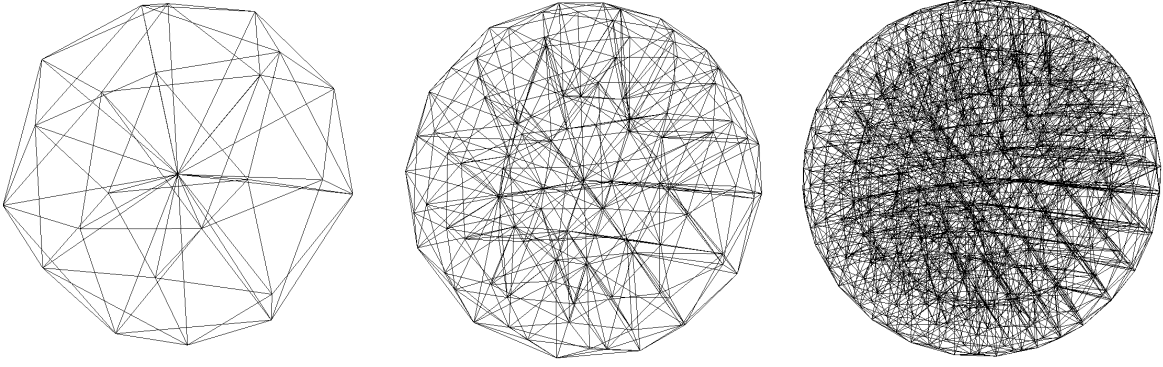


Figure A6: Tetrahedral approximations of a unit sphere with, from left to right, decreasing values of  $h$ , created with Gmsh [GR09].

The bulk and surface finite element spaces are given by

$$\begin{aligned} \mathbb{V}_{h,Y} &= \{ \Psi \in C(Y_h) : \Psi|_K \text{ is linear affine for each } K \in S_h \}, \\ \mathbb{V}_{h,\Gamma} &= \{ \Psi \in C(\Gamma_h) : \Psi|_R \text{ is linear affine for each } R \in S_h \text{ with } R = K \cap \Gamma_h \neq \emptyset \}. \end{aligned}$$

The bulk space is spanned by nodal basis functions defined by

$$\chi_j \in \mathbb{V}_{h,Y}, \quad \chi_j(X_k) = \delta_{jk} \quad \text{for } j, k = 1, \dots, J,$$

where  $\delta_{jk}$  is the Kronecker delta and  $J$  is the number of nodes (vertices)  $X_j \in Y$  of the tetrahedrons  $S_h$ . Then function  $\Phi(t) \in \mathbb{V}_{h,Y}$  has the form

$$\Phi(t, x) = \sum_{j=1}^J a_j(t) \chi_j(x) \quad \text{for } x \in Y_h, t \in (0, T),$$

with real measurable functions  $a_j$ . Similarly the surface finite element space is spanned by nodal basis functions

$$\mu_j \in \mathbb{V}_{h,\Gamma}, \quad \mu_j(Z_k) = \delta_{jk} \quad \text{for } j, k = 1, \dots, M,$$

where  $Z_j \in \Gamma$ , with  $j, k = 1, \dots, M$ , are nodes of the triangulated surface such that  $Z_k = X_k \cap \Gamma_h \neq \emptyset$ . Then function  $P(t) \in \mathbb{V}_{h,\Gamma}$  has the form

$$P(t, x) = \sum_{j=1}^M b_j(t) \mu_j(x) \quad \text{for } x \in \Gamma_h, t \in (0, T),$$

with real measurable functions  $b_j$ . Thus, the semi-discretized problem corresponding to (3)-(6) reads

$$\begin{aligned}
& \langle \partial_t \Phi_d, \Psi \rangle_{Y_h} + \langle D_1 \nabla \Phi_d, \nabla \Psi \rangle_{Y_h} + \langle C_1 \text{tr}(\sigma(U))_+ \Phi_d, \Psi \rangle_{Y_h} + \langle k_3 \Phi_d, \Psi \rangle_{\Gamma_h} = \langle k_1 \Phi_a, \Psi \rangle_{Y_h}, \\
& \langle \partial_t \Phi_a, \Psi \rangle_{Y_h} + \langle D_2 \nabla \Phi_a, \nabla \Psi \rangle_{Y_h} + \langle k_1 \Phi_a, \Psi \rangle_{Y_h} = \langle C_1 \text{tr}(\sigma(U))_+ \Phi_d, \Psi \rangle_{Y_h} + \langle k_3 \Phi_d, \Psi \rangle_{\Gamma_h}, \\
& \langle \partial_t P_a, W \rangle_{\Gamma_h} + \langle D_3 \nabla_{\Gamma_h} P_a, \nabla_{\Gamma_h} W \rangle_{\Gamma_h} + \langle k_4(\Phi_a) P_a, W \rangle_{\Gamma_h} = \langle k_5(\Phi_a), W \rangle_{\Gamma_h}, \\
& \langle E(\Phi_a) \epsilon(U), \epsilon(V) \rangle_{Y_h} = \langle \mathbb{P}(k_6 P_a \hat{\nu}), V \rangle_{\Gamma_h},
\end{aligned} \tag{9}$$

for every test function  $\Psi \in \mathbb{V}_{h,Y}$ ,  $W \in \mathbb{V}_{h,\Gamma}$  and  $V \in \mathbb{V}_{h,Y}$ .

To obtain the fully discrete problem we discretize (9) in time using the backwards Euler method with

$$\partial_t \Phi \approx \frac{\Phi^n - \Phi^{n-1}}{\Delta t},$$

where  $\Delta t = T/N$ , and an IMEX time-stepping method, in which the diffusion term is treated implicitly and the nonlinear reaction terms are treated explicitly [LMV13]. The discrete system, with the notation  $\Phi^n(x) = \Phi(t_n, x)$ , reads

$$\begin{aligned}
& \langle E(\Phi_a^{n-1}) \epsilon(U^n), \epsilon(V) \rangle_{Y_h} = \langle \mathbb{P}(k_6 P_a^{n-1} \hat{\nu}), V \rangle_{\Gamma_h}, \\
& \Delta t^{-1} \langle \Phi_d^n, \Psi \rangle_{Y_h} + \langle D_1 \nabla \Phi_d^n, \nabla \Psi \rangle_{Y_h} + \langle C_1 \text{tr}(\sigma(U^n))_+ \Phi_d^n, \Psi \rangle_{Y_h} + \langle k_3 \Phi_d^n, \Psi \rangle_{\Gamma_h} \\
& \quad = \Delta t^{-1} \langle \Phi_d^{n-1}, \Psi \rangle_{Y_h} + \langle k_1 \Phi_a^{n-1}, \Psi \rangle_{Y_h}, \\
& \Delta t^{-1} \langle \Phi_a^n, \Psi \rangle_{Y_h} + \langle D_2 \nabla \Phi_a^n, \nabla \Psi \rangle_{Y_h} + \langle k_1 \Phi_a^n, \Psi \rangle_{Y_h} \\
& \quad = \Delta t^{-1} \langle \Phi_a^{n-1}, \Psi \rangle_{Y_h} + \langle C_1 \text{tr}(\sigma(U^n))_+ \Phi_d^n, \Psi \rangle_{Y_h} + \langle k_3 \Phi_d^n, \Psi \rangle_{\Gamma_h}, \\
& \Delta t^{-1} \langle P_a^n, W \rangle_{\Gamma_h} + \langle D_4 \nabla_{\Gamma_h} P_a^n, \nabla_{\Gamma_h} W \rangle_{\Gamma_h} + \langle k_4(\Phi_a^n) P_a^n, W \rangle_{\Gamma_h} \\
& \quad = \Delta t^{-1} \langle P_a^{n-1}, W \rangle_{\Gamma_h} + \langle k_5(\Phi_a^n), W \rangle_{\Gamma_h}.
\end{aligned} \tag{10}$$

To benchmark the numerical scheme and implementation in FEniCS, we consider  $Y$  to be a unit ball and a simplified model

$$\begin{aligned}
& -\nabla \cdot \sigma(u) = f && \text{in } Y, \\
& \sigma(u) \cdot \nu = \mathbb{P}(g\rho) && \text{on } \Gamma, \\
& \partial_t \phi - \Delta \phi = q_1 + \text{tr}(\sigma(u))_+ && \text{in } Y, t > 0, \\
& \nabla \phi \cdot \nu = \rho - \phi && \text{on } \Gamma, t > 0, \\
& \partial_t \rho - \Delta \rho = q_2 - \rho + \phi && \text{on } \Gamma, t > 0.
\end{aligned} \tag{11}$$

The functions  $f$ ,  $g$  and  $\rho$  are such that

$$\begin{aligned}
u_{ex}(x, t) &= (2x_1^2 x_2 x_3 e^{-4t}, -x_1 x_2^2 x_3 e^{-4t}, -2x_1 x_2 x_3^2 e^{-4t}), \\
\phi_{ex}(x, t) &= \cos(x_1 x_2 x_3) e^{-4t},
\end{aligned}$$

is the exact solution of (11). Then for the experimental order of convergence

$$\text{EOC} = \frac{\log(e_n/e_{n-1})}{\log(h_n/h_{n-1})},$$

where  $h_n$ , for  $n = 1, 2, 3, 4$ , are given in Table (A2) and  $e_n$  is the error in the  $L^2$ -norm or the  $H^1$ -norm, we obtain the second order of convergence in the  $L^2$ -norm and first order of convergence in  $H^1$ -norm, see Table A3.

$$| 0.64009064 | 0.51659533 | 0.26133991 | 0.13143219 |$$

Table A2: Four mesh sizes used in the calculation of EOC.

EOC for L2 norm for $\phi$	1.63892969	1.77954013	1.93991995
EOC for H1 norm for $\phi$	1.44823967	1.68924575	1.89210920
EOC for L2 norm for $\rho$	1.58078852	1.78119701	1.96179159
EOC for H1 norm for $\rho$	1.78659381	1.49338646	1.52956398
EOC for L2 norm for $u$	0.92059071	1.74758321	1.87989078
EOC for H1 norm for $u$	1.05358979	1.40005535	1.27787725

Table A3: Experimental order of convergence for numerical scheme (10) considered for model (11).

#### A.4 Conversion from $\mu M$ to $\#/\mu m^2$

Scott et al. [SFR21] uses  $\mu M$  for concentrations in the cytoplasm and  $\#/\mu m^2$  for concentrations on the plasma membrane, specifically for  $\rho_a$ . In the model derived and analysed in Section 2 we use  $\mu M$  for all concentrations, equivalent to  $10^{-3} \frac{\text{mol}}{\text{m}^3}$  for concentrations in the cytoplasm and to  $10^{-9} \frac{\text{mol}}{\text{m}^2}$  for  $\rho_a$ . To be able to use the same initial conditions and to compare the results, we need to find a conversion from  $\#/\mu m^2$  to  $\mu M$ . We use the fact that the maximum value for  $\rho_a$  for large  $E$  is  $11 \cdot 10^{-16} \mu\text{mol}/\mu\text{m}^2$  as given in [SFR21, Figure 2B]. The maximum value of the numerical results for  $\rho_a$  for large  $E$  is  $593 \#/\mu\text{m}^2$  as given in [SFR21, Figure 3C(ii)] and assume these are equivalent. This relation gives the conversion

$$10^{-9} \frac{\text{mol}}{\text{m}^2} = 10^{-15} \frac{\mu\text{mol}}{\mu\text{m}^2} = \frac{5930}{11} \#/\mu\text{m}^2 = 539.09 \#/\mu\text{m}^2. \quad (12)$$

#### A.5 Simulations with nucleus

To model the inclusion of a nucleus in the cell, consider the model equations (3) and (6) in  $Y \setminus \bar{Y}_{\text{nc}}$ , where domain  $Y_{\text{nc}}$  represents the nucleus. We choose zero flux boundary conditions for  $\phi_d$  and  $\phi_a$  on  $\partial Y_{\text{nc}}$ . For the mechanics, we choose the interior boundary condition to model the fact that the nucleus is hard to deform

$$\sigma(u) \cdot \nu = -\omega u \quad \text{on } \partial Y_{\text{nc}}, \quad (13)$$

where  $\omega$  is a positive constant determining the rigidity of the nucleus.

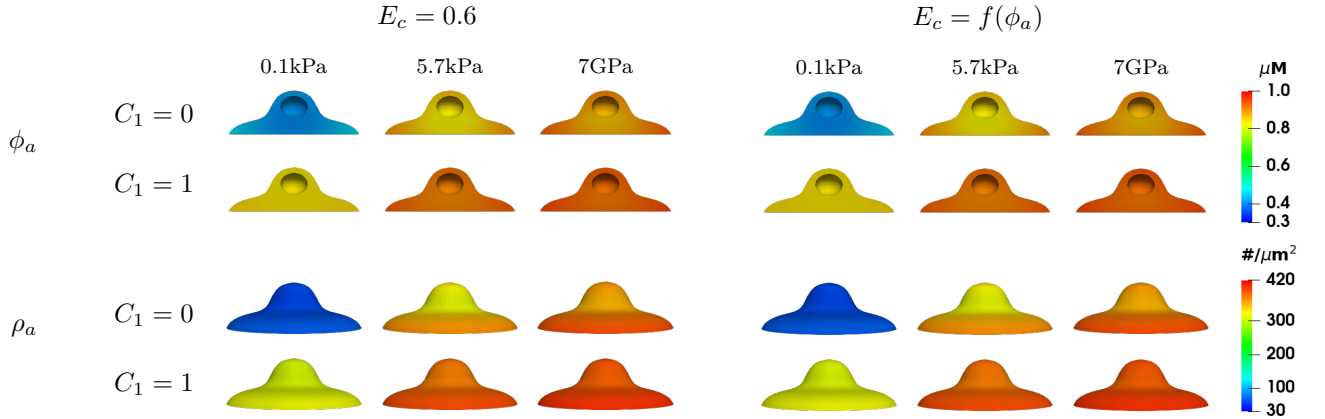


Figure A7: Numerical simulation results of Appendix A.5 showing  $\phi_a$  and  $\rho_a$  for model (3), (4), (6), and (13) for the radially symmetric shape with a nucleus and in the case of the 3D stimulus at steady state for  $T = 100$  s. Within each figure the columns are  $E = 0.1, 5.7, 7 \cdot 10^6$  kPa and parameter values as in Tables 1 and 2, and  $\omega = 1$ . The corresponding results without a nucleus can be found in Figure 11.

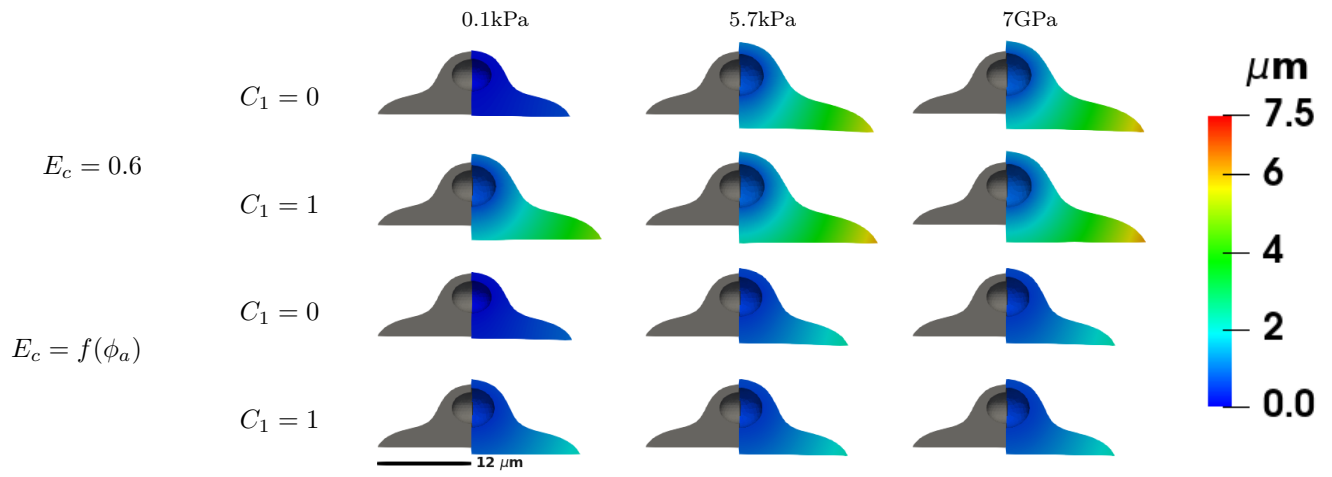


Figure A8: Numerical simulation results of Appendix A.5 showing  $u$  for model (3), (4), (6), and (13) for the radially symmetric shape with a nucleus and in the case of the 3D stimulus at steady state for  $T = 100$  s. Within each figure the columns are  $E = 0.1, 5.7, 7 \cdot 10^6$  kPa and parameter values as in Tables 1 and 2, and  $\omega = 1$ . The corresponding results without a nucleus can be found in Figure 12.